Quarterly Report for

Contract DE-FG36-02ID14418

Stanford Geothermal Program

July-September 2005

Table of Contents

1. MEASUREMENTS OF IN-SITU WATER SATURATION IN GEOTHERMAL ROCKS

This project is being conducted by Research Assistant Aysegul Dastan, Senior Research Engineer, Kewen Li and Prof. Roland Horne. The objective is to study the effects of pressure, temperature and permeability on in-situ water saturation in fractured geothermal reservoirs.

1.1 SUMMARY

Knowledge of immobile and in-situ water saturation and porosity is essential for characterization of geothermal fields and determining their exploitative capacities. Traditionally, numerical simulations based on field measurements have been used for this purpose. Direct measurement of irreducible water saturation is very useful as well. Direct measurement involves the in-situ measurement of pressure and water content of a rock sample at high temperature and pressure. This allows for a direct comparison between water saturation values inferred from simulations and measured saturation values, and permits a better understanding of the geothermal field.

Earlier, as part of a California Energy Commission (CEC) project, water saturation at The Geysers geothermal field has been studied (Horne et al., 2003). In that work, both numerical simulations and direct measurements were made and presented comparatively. The study developed an X-ray CT method for the direct measurement of water saturation in a core sample from The Geysers. This technique needs to be modified to circumvent some of the experimental artifacts (i.e., beam hardening effects during CT scans) and more measurements need to be taken for a better characterization of The Geysers rock sample and of samples from other fractured geothermal rocks.

The objective in this project is to improve and extend the in-situ measurement method for direct characterization. For that, we are first using the same Geysers rock sample that was analyzed previously, and will subsequently compare it to other geothermal formations. We would like to develop a systematic procedure to characterize geothermal rocks. In earlier reports we focused on analyzing and modifying the experimental apparatus used by Horne et al. (2003). The report of Spring 2005 included the detailed procedure to detect the location of leaks, and two different characterization methods. The first was an application of the pressure pulse decay method to measure the permeability. Since we did not know some of the equipment parameters precisely, the result we obtained gave only order-of-magnitude information about the permeability. In that report we also mentioned the preparation of the core for CT scanning. At that time we had some technical difficulties with the CT scanner and hence we were not able to provide any of the CT scan results.

In this report we summarize our progress during Summer 2005 and present and evaluate our results. In the preliminary measurements that we will mention here, we were not able to reproduce the results of Horne et al. (2003), although we used average values to process the CT scans (i.e., using average CT values). The data collected is still being processed for a better evaluation. We would like to analyze the data and, if needed, obtain another set of measurements to characterize the sample. In particular, we would like to investigate the large irreducible water saturation value measured before. We would like to confirm that

value and understand the reasons behind this observation and its possible consequences to reservoir performance.

1.1.1 Characterization of the rocks: S_w and ϕ parameters

In-situ characterization consists of taking X-ray computer tomography (CT) images of a rock sample under various pressure and temperature conditions. Here, the objective is to determine the saturation and porosity values, S_w and ϕ, respectively. The CT instrument scans the sample and finds the distribution of water in the sample. Figure 1.1 shows two scans, one for which the core was dried and the other for which the sample was saturated with water at room temperature. The grayscale pictures show the distribution of CT values in a cross section of the core holder. Analyzing such images, water saturation can be found from the measured CT values. $CT_{wet}(T)$, $CT_{dry}(T)$ are the CT values of the core sample when it is completely saturated by water and when the sample is vacuumed to a completely empty condition, respectively. The difference between the two gives the relative spatial distribution of water in the 100% water saturation case. At a test condition, there will be a mixture of water and steam within the core. Then, the difference between $CT_{exp}(T)$ and $CT_{dry}(T)$ gives a relative measure of water distribution within the core. From Eq. 1.1 one can find the water saturation:

$$S_w = \frac{CT_{\exp}(T) - CT_{dry}(T)}{CT_{wet}(T) - CT_{dry}(T)} \tag{1.1}$$

Figure 1.1: CT dry scan (left) and CT wet scan (right). From average values within the core, CT_{dry}=1486 CT_{wet}=1511.

Similarly, the porosity of the core sample can be found using Eq. 1.2. Here, CT_{water} and CT_{air} are the CT numbers of water and air, respectively.

$$\phi = \frac{CT_{wet}(T) - CT_{dry}(T)}{CT_{water}(T) - CT_{air}(T)} \tag{1.2}$$

Using CT_{water} = 0, CT_{air}= -1000, CT_{dry}=1486, and CT_{wet}=1511 (from Figure 1) we can find the average porosity to be 0.025 in this example. We will discuss in detail how to get the CT images and evaluate them later.

1.1.2 Experimental Apparatus

The apparatus used in the experiment brings the core to the desired temperature and pressure conditions, and injects or drains water as necessary. A schematic of the apparatus is shown in Figure 1.2; the inset shows the core holder. The core was machined and inserted in an aluminum cylinder filled with high-temperature epoxy, which was then cured at 160 °C. To control the temperature in the core, a silicone oil bath is used. The oil is maintained at a controlled temperature and is passed through an external aluminum coil around the core holder. The use of aluminum is essential because it is relatively transparent to the X-rays that are used for the CT imaging. We also applied thermal insulation around the aluminum coil. Again, the insulation material is put together using aluminum tapes and the core is wrapped with aluminum foil after the insulation is applied. The insulation helps keep the temperature constant and uniform within the core.

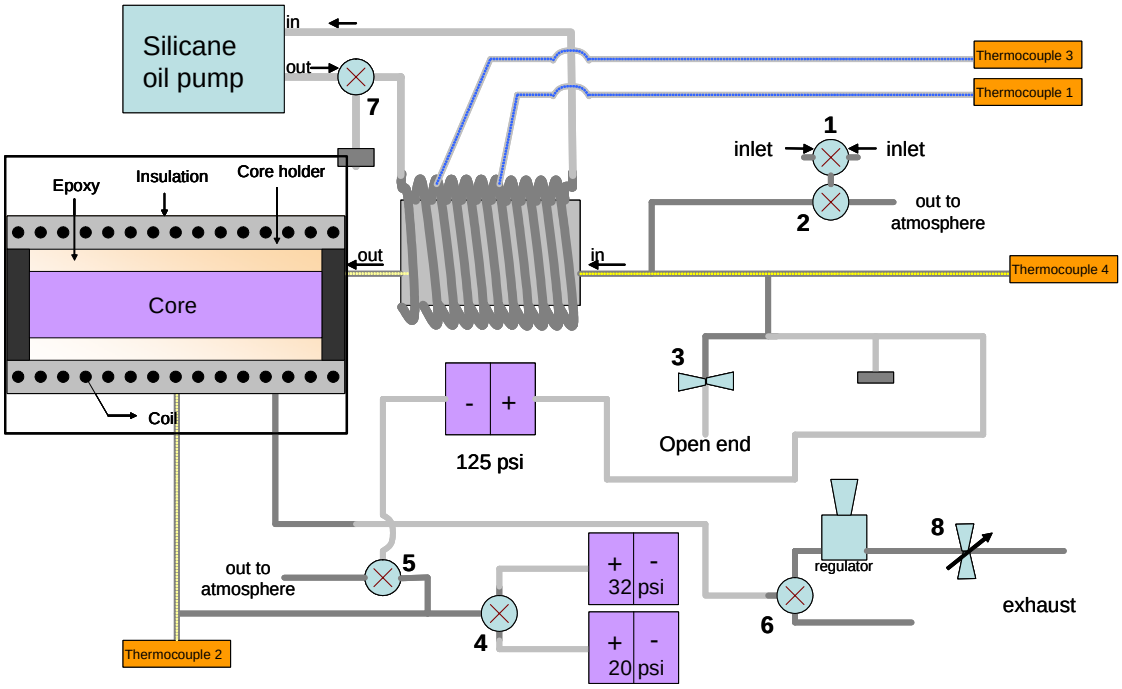

Figure 1.2: Schematic of the apparatus (inset is the core holder).

In the apparatus, the vacuum pump is used to remove the air in the core sample such that a steam-water environment can be established. Water is delivered using a water pump. The amount of the water entering and leaving the sample can be recorded in the computer using a LabView-based data acquisition interface.

1.1.3 Measurement Procedure

Our aim is to measure CT_{dry}, CT_{wet}, and the CT_{exp} values that are needed to calculate the S_w and ϕ parameters using Equations 1.1 and 1.2. In this section we will summarize the steps we take for a standard test.

Drying the core: First, with all the valves open to the atmosphere, the system is dried by bringing the temperature up to 80-100 °C. Then, the oil circulation is turned off, the valves are closed and vacuum pump is connected to the system from the exhaust side, bypassing the regulator (valve #6 in Figure 1.2). Vacuum is pulled until the pressure drops somewhere around 60-100 mTorr. This process usually takes about two days. Also, vacuuming should be repeated when the apparatus is in the CT scanner, just before the first scan. In this case, however, the pressure should drop down to 60-100 mTorr level within a couple of hours. If that does not happen, it is worth checking the oil of the vacuum pump and replacing it if necessary. Vacuuming also ensures the system is leak-free.

After the system is placed in the scanner, one should take a couple of measurements to see if there is any X-ray beam hardening effects. The idea is to use just one cross-section to represent the core. By placing the sample at an angle to achieve a diagonal cross-section, we were able to avoid the beam hardening effect.

Due to the range of pressures of interest, we make the main pressure measurement using the 125 psi differential transducer. It is very important during drying to ensure that the negative end of this transducer is vacuumed properly for a correct reading of system pressure.

The CT measurement taken at this point gives the CT_{dry} value.

Saturating the core with water: To avoid corrosion, one needs to use deionized (DI) water for saturation. The flask is half-filled with water and vacuum is applied to the flask system for about half an hour. The idea here is to suck out the air dissolved in water. Then the flask is connected to the vacuumed system such that no air is let inside. This is done while the vacuum is still connected to the system. The vacuum pump is connected to valve 6 and the flask is connected to valve 1. First, valve 2 is opened to vacuum the system again (for about 40 mins). Valve 1 is then opened to let the water in. The vacuum is decoupled from the system as soon as water is observed at the output. Then, we wait until the reading on the balance carrying the flask stabilizes. This means that no more water can enter the system by itself. The next step is to use the water pump to let more water in. The water to be used with the water pump is prepared in the same way as the water used in the flask. The water pump is connected to valve 1 as well. The water pump should run until the system pressure reaches 50 psi. It is important to increase the system pressure before heating to avoid steam formation as the system is heated up. It is useful to flush the system with water to ensure there is no air trapped inside the system.

The scan taken at this point is the CT_{wet} scan.

Heat up: The oil circulation temperature is increased to 120 °C by 20 °C intervals, starting from 80 °C. It is important to watch the pressure during heat up and ensure that it lies between the boiling point at 120 °C and 50 psi. Pressures above 50 psi may result in leaks or some other failure in the system. If pressure approaches 50 psi, it should be reduced by adjusting the regulator. To avoid the pressure decreasing more than intended, we also added a needle valve after the regulator. With this additional control, we were able to

decrease the pressure as planned. While heating up, we took CT scans as well to see how the saturation changed as a function of temperature.

Pressure blowdown test: After the system stabilizes at 120 °C, we start to decrease the pressure through the regulator. Once the pressure is decreased to some value, it is important to wait long enough to let the system stabilize, sometimes up to 36 hours. Since we did not know the boiling point exactly we decreased the pressure by small steps after we were around 25 psi (see Figures 1.5-1.8). Note that at the boiling point, the saturation changes abruptly.

In our case there was noise in the pressure readings from the transducer, making it difficult to understand whether the system stabilized by just looking at the current reading. (The reading varied within an interval of 1 psi). For that reason, we took an average of the last 100 pressure values logged to even out the effects of the noise. To conclude whether the system had stabilized, we plotted pressure as a function of time. We obtained CT scans after each stabilization phase. Our aim was to reproduce the results of Horne et al. (2003), which are plotted in Fig 1.3. Irreducible water saturation is determined by the abrupt drop in saturation as the pressure is decreased. From that point on, the saturation decreases linearly with pressure.

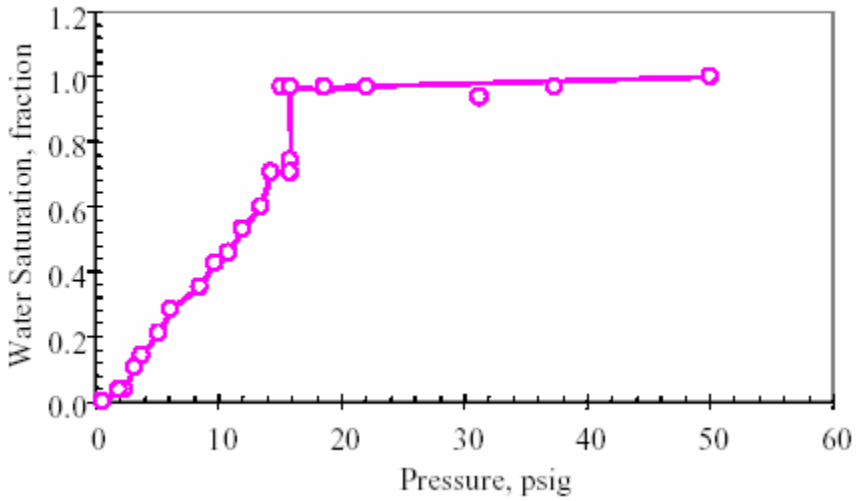

Figure 1.3:Variation of in-situ water saturation in The Geysers rock with pressure at a temperature of 120℃. (Horne et al. , 2003).

1.2 EXPERIMENTAL RESULTS

As explained in Section 1.1.3, we made CT scans of a cross section of the Geysers sample at various temperature and pressure conditions.

1.2.1 Computer Tomography Essentials

Computer tomography (CT) is a medical imaging technique that uses X-rays to produce images of thin slices of any part of the human body. We can use the same procedure to measure information about the water content of rock samples. We made the measurements using a Picker^{TM} Synerview X-ray CT scanner (Model 1200 SX), which was designed originally for medical purposes. The sample holder is placed within the gantry, which is a large ring as seen in Figure 1.4. The ring contains the X-ray tube and the X-ray detectors. During a CT scan, the X-ray tube makes a complete rotation around the core. The X-ray beam is collimated to the slice of the sample being imaged. At any instant of time during the scan, this beam of X-rays is attenuated by the sample. Different parts of the beam are attenuated by varying amounts, depending on the types and amounts of material the X-rays pass through. Water-saturated rock attenuates X-rays differently than unsaturated rock. Once the different parts of the X-ray beam pass through the sample and are attenuated, their remaining intensity is measured by an arc of about 500 X-ray detectors. These X-ray measurements at the detectors are repeated hundreds of times during the scan as the X-ray tube sends X-rays through the sample at different angles. The X-ray detectors produce electronic pulses proportional to the X-ray intensity they receive. These hundreds of thousands of data pulses, from different detectors and at different positions of the X-ray tube, are fed into a computer which uses them to form a digital image of the slice of the sample through which the X-rays passed. In creating the image, the computer assigns each pixel a number between -1000 and about +3000. This is called the pixel's CT number. The larger the CT number the greater the attenuation of the tissue represented within that pixel and the brighter that pixel will appear in the image. By definition, air has a CT number of -1000 and water has a CT number of zero. Therefore it is possible to deduce by how much the sample is saturated and measure the saturation as a function of other variables.

1.2.2 Experimental Results based on average CT values

The CT scanner provides CT values for all the points in the cross section. This gives us important information about the distribution of water within the sample. However, since we are interested in the overall water saturation, we can obtain useful information to a first order by comparing the average CT values. We will look into how position dependence can be taken into account in the next section.

As explained in Section 1.1.1, we would like to measure $CT_{wet}(T)$, $CT_{dry}(T)$, and $CT_{exp}(T)$ values. Figure 1.4 shows the experimental apparatus we used for these measurements. In the picture, the apparatus has been placed in the CT scanner.

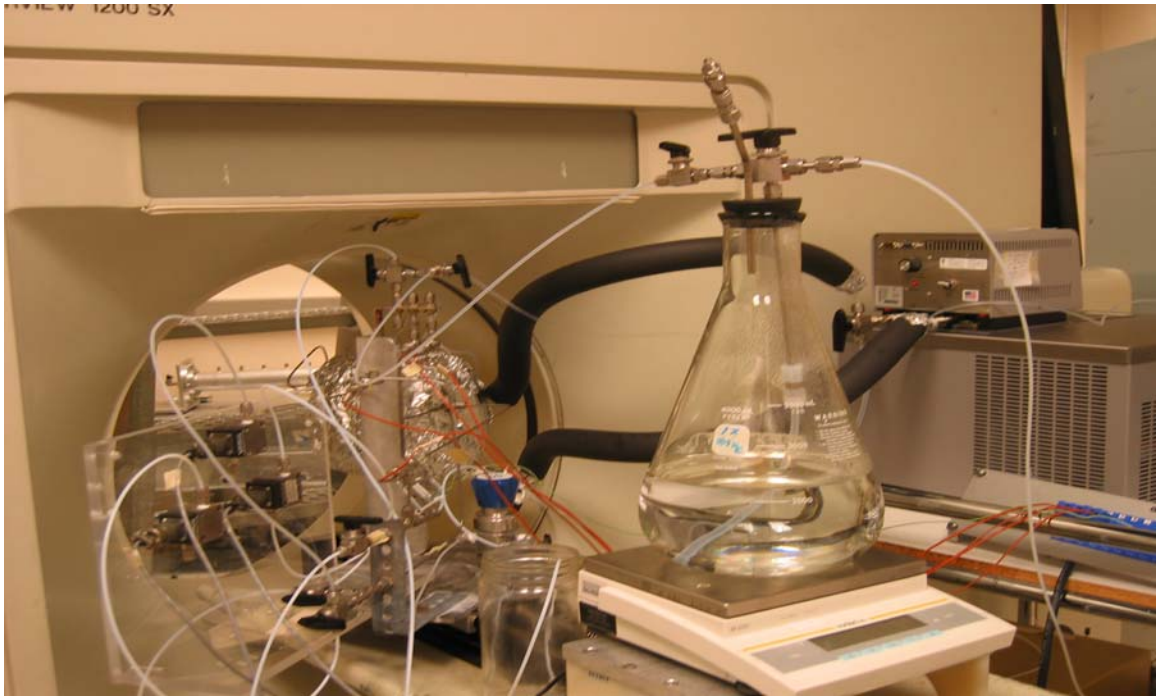

Figure 1.4: Apparatus in the CT scanner.

We took a number of CT images during heat-up and pressure blowdown tests. Table 1.1 tabulates the images taken, pressure readings when those scans were made, and average CT values. Figures 1.5 through 1.8 show the pressure variation during the blowdown test. The graphs are plotted with respect to time. The corresponding relative time of the measurements is also listed in the table, which allows for determination of which measurements were taken at stable values, with a cross check with Figures 1.5-1.8. Note that to eliminate the uncertainty introduced by the noise in the transducer readings, the pressure values tabulated are the averaged pressure values. The averaging is also done on the pressure graphs to eliminate the noise. Here, a moving average of 100 data points is used. Data was logged every second. Using a moving average filter smoothes the curve for a better visual analysis.

Table 1.1: CT values and their corresponding pressure and temperature.

file	Date	time	Rel time (hr)	CT value	Pavg (psi)	T (C)
320.04	Aug 1st 2005	10:47	NA	1486	NA	25
320.05	Aug 2nd 2005	13:50	NA	1511	NA	25
320.06	Aug 7th 2005	18:30	NA	1515	NA	25

320.07	Aug 8th 2005	9:04	NA	1428	NA	25
320.08	Aug 10th 2005	14:44	NA	1429	NA	25
320.09	Aug 11th 2005	15:40	NA	1429	NA	60
320.10	Aug 11th 2005	17:53	NA	1427	NA	65
320.11	Aug 12th 2005	3:01	NA	1431	NA	75
320.12	Aug 12th 2005	3:11	NA	1431	NA	75
320.13	Aug 12th 2005	9:08	NA	1423	NA	90
320.14	Aug 12th 2005	12:33	NA	1425	NA	110
320.15	Aug 12th 2005	15:38	NA	1428	NA	120
320.16	Aug 14th 2005	21:40	NA	1430	NA	120
320.17	Aug 15th 2005	11:12	2.12	1425	45.42	120
320.18	Aug 15th 2005	13:32	4.44	1418	30.1	120
320.19	Aug 15th 2005	14:10	5.09	1423	23.98	120
320.20	Aug 15th 2005	22:02	12.96	1426	21.89	120
320.21	Aug 16th 2005	8:44	23.65	1424	21.48	120
320.22	Aug 16th 2005	15:08	30.05	1423	19.78	120
320.23	Aug 16th 2005	15:17	30.21	1423	19.68	120
320.24	Aug 17th 2005	9:05	48	1425	16.17	120
320.25	Aug 17th 2005	9:19	48.24	1423	16.13	120
320.26	Aug 17th 2005	9:54	48.83	1420	14.23	120
320.27	Aug 17th 2005	10:55	49.83	1423	14.55	120

320.28	Aug 17th 2005	12:50	51.75	1426	14.29	120
320.29	Aug 17th 2005	14:38	53.55	1423	14.2	120
320.30	Aug 19th 2005	12:21	99.26	1427	15.53	120
320.31	Aug 19th 2005	16:19	103.23	1427	15.59	120
320.32	Aug 20th 2005	21:12	132.11	1429	14.66	120
320.33	Aug 21st 2005	22:32	169.44	1424	13.94	120
320.34	Aug 21st 2005	22:45	169.67	1426	13.5	120
320.35	Aug 23rd 2005	0:16	195.18	1425	13.17	120
320.36	Aug 23rd 2005	11:27	206.36	1424	12.93	120
320.37	Aug 23rd 2005	17:04	211.98	1427	12.9	120
320.38	Aug 24rd 2005	16:14	235.14	1431	12.3	120
320.39	Aug 24rd 2005	16:15	235.17	1429	12.3	120
320.40	Aug 25th 2005	0:42	243.61	1432	12.28	120
320.41	Aug 25th 2005	0:44	243.65	1432	12.28	120
320.42	Aug 25th 2005	12:23	255.3	1425	11.43	120
320.43	Aug 25th 2005	17:35	260.49	1434	11.4	120
320.44	Aug 25th 2005	17:36	260.51	1433	11.4	120
320.45	Aug 25th 2005	18:04	260.98	1428	11.29	120
320.46	Aug 26th 2005	13:02	279.94	1434	10.89	120
320.47	Aug 26th 2005	15:34	282.48	1436	10.99	120
320.48	Aug 27th 2005	2:02	292.94	1437	11.04	120

320.49	Aug 28th 2005	1:16	316.17	1438	10.98	120
320.50	Aug 28th 2005	1:17	316.19	1437	10.98	120
320.51	Aug 28th 2005	1:18	316.21	1436	10.99	120
320.52	Aug 28th 2005	1:24	316.31	1433	10.64	120
320.53	Aug 28th 2005	1:30	316.41	1436	10.21	120
320.54	Aug 28th 2005	1:34	316.47	1437	9.88	120
320.55	Aug 28th 2005	10:54	325.81	1426	10.28	120
320.56	Aug 28th 2005	21:38	336.54	1434	10.25	120
320.57	Aug 28th 2005	21:40	336.57	1424	10.24	120
320.58	Aug 28th 2005	21:54	336.81	1426	10.32	120
320.59	Aug 28th 2005	22:13	337.12	1427	8.43	120
320.60	Aug 29th 2005	13:14	352.14	1417	8.38	120
320.61	Aug 29th 2005	13:15	352.16	1424	8.38	120
320.62	Aug 29th 2005	16:35	355.49	1432	8.43	120
320.63	Aug 29th 2005	16:36	355.51	1427	8.42	120
321.01	Aug 30th 2005	9:24	372.31	1415	8.09	120
321.02	Aug 30th 2005	9:25	372.32	1423	8.11	120
321.03	Aug 30th 2005	23:51	386.75	1434	4.86	120
321.04	Aug 30th 2005	23:56	386.84	1434	4.83	120
321.05	Aug 31th 2005	11:05	397.99	1425	4.67	120
321.06	Aug 31th 2005	11:06	398	1423	4.65	120

321.07	Aug 31th 2005	11:08	398.04	1423	4.65	120
321.08	Aug 31th 2005	11:16	398.17	1426	0.54	120
321.09	Sep 1st 2005	11:09	422.05	1423	2.29	120
321.10	Sep 1st 2005	11:10	422.07	1422	2.29	120
321.11	Sep 1st 2005	11:16	422.17	1423	0.045	120
321.12	Sep 1st 2005	13:04	423.97	1426	-0.31	120
321.13	Sep 2nd 2005	12:00	446.9	1419	-0.43	120
321.14	Sep 2nd 2005	12:01	446.92	1429	-0.44	120
321.15	Sep 2nd 2005	14:01	448.92	1423	-0.39	120

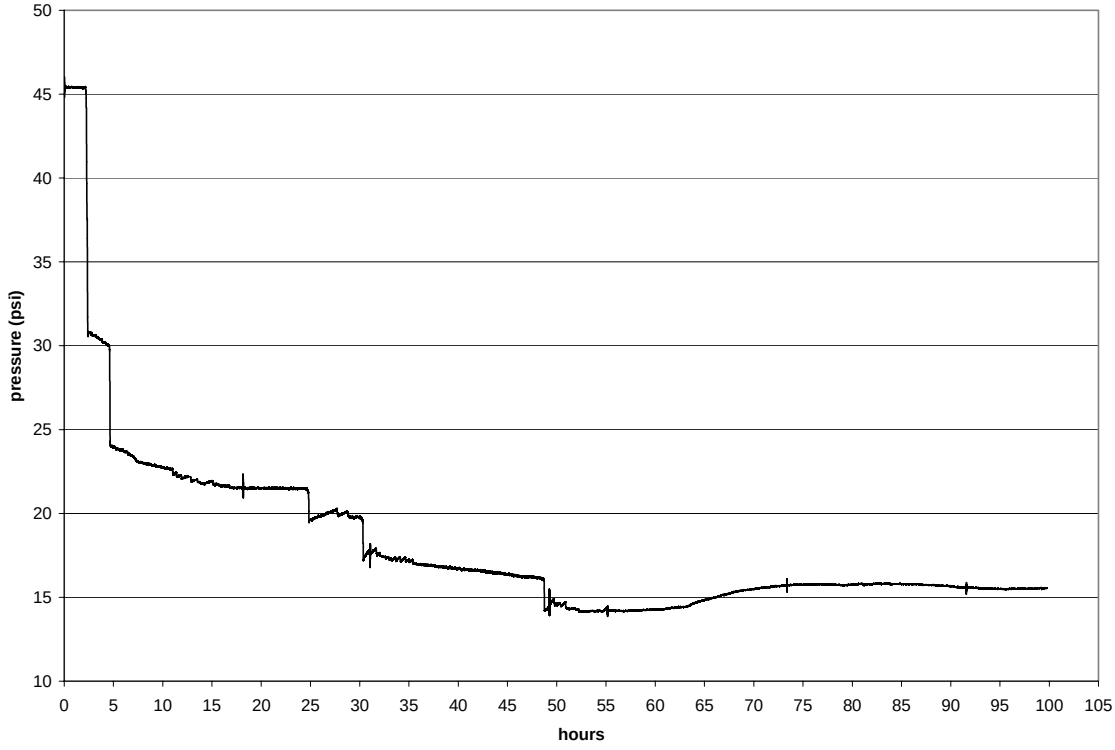

Figure 1.5: Pressure transient data (part 1).

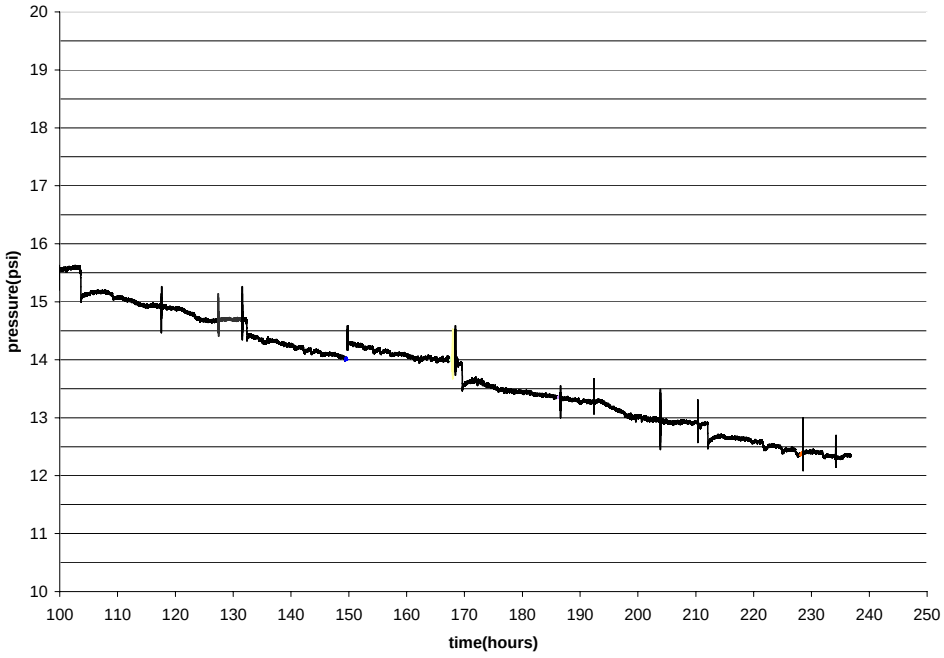

Figure 1.6: Pressure transient data (part 2).

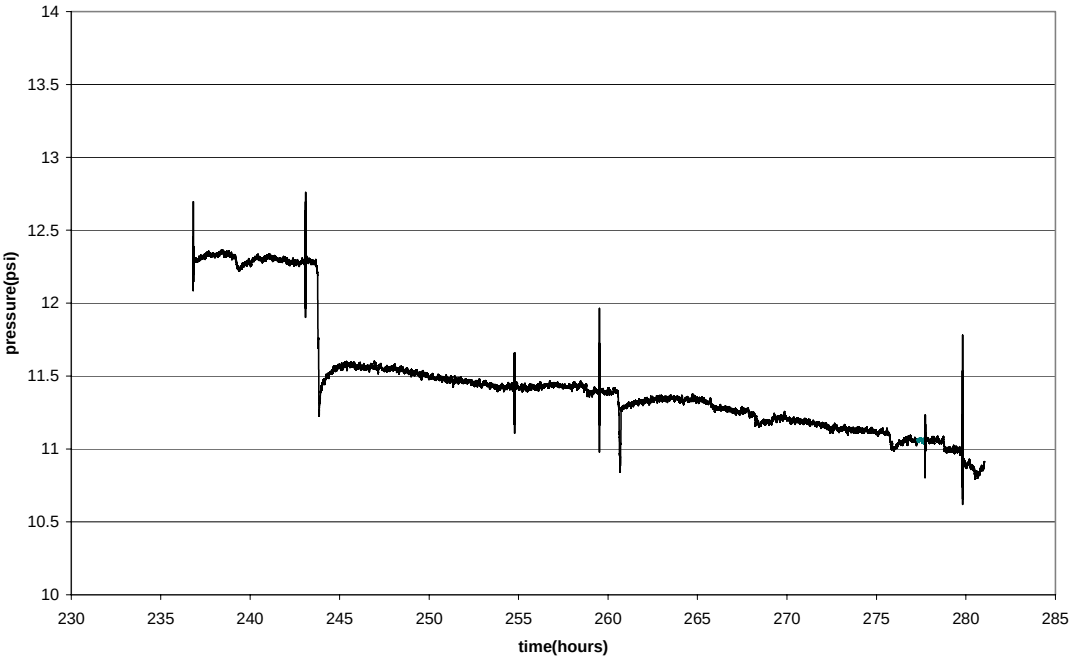

Figure 1.7Pressure transient data (part 3).

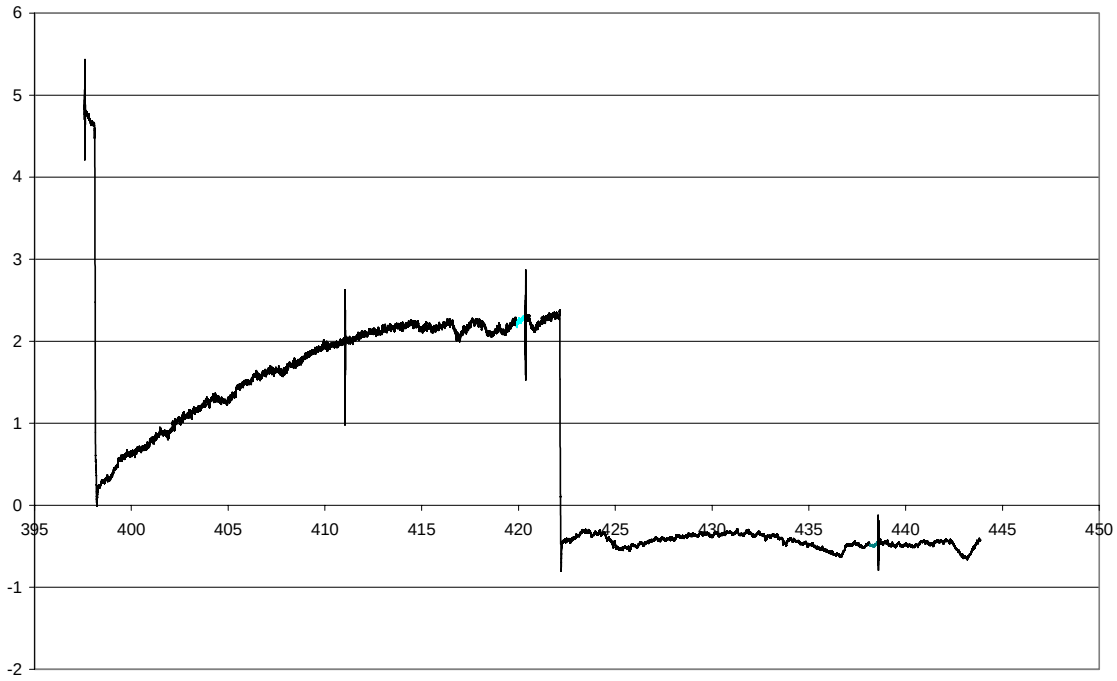

Figure 1.8: Pressure transient data (part 4).

Figure 1.9 plots saturation as a function of temperature. As temperature is increased, saturation decreases. During temperature increase, we let some water out to keep the pressure within 30-50 psi. Therefore such a decrease in saturation is expected. These data were taken without stabilization. Indeed, at that pressure the water is single phase and so stabilization does not take long. However, average CT values were used for this experiment. A ±1 variation in average CT values may change the saturation by 5%. This should also be taken into account when these data is evaluated.

Figure 1.10 shows the saturation as a function of pressure. For this plot, only saturations corresponding to stabilized pressures are included. That is because as the pressure is decreased the system enters the two-phase region. In that region, at a certain temperature, there is a dynamic equilibrium between the liquid phase and the vapor phase. After each pressure drop, we have to wait sufficiently until the system stabilizes. From Figures 1.5 – 1.8, we see that this stabilization time can be up to 48 hours. If the system is not stabilized, the amount of water phase will change even during one scan. This will result in inaccurate saturation readings.

Figure 1.10 shows a behavior different than the earlier study shown in Figure 1.3. As the pressure was decreased, we notice the saturation pressure to be around 11-11.5 psi, which is lower than the anticipated value of 14.3 psi. We can see the saturation pressure from Figure 1.7: as the pressure is decreased, the system immediately responds in such a way to reverse that change. Also there are multiple saturation values corresponding to the same pressure in the S_w vs. p graph. The reason there is ambiguity in the S_w vs. p graph is mostly due to our using average CT values over a large area. We believe a better analysis of the data may yield better data.

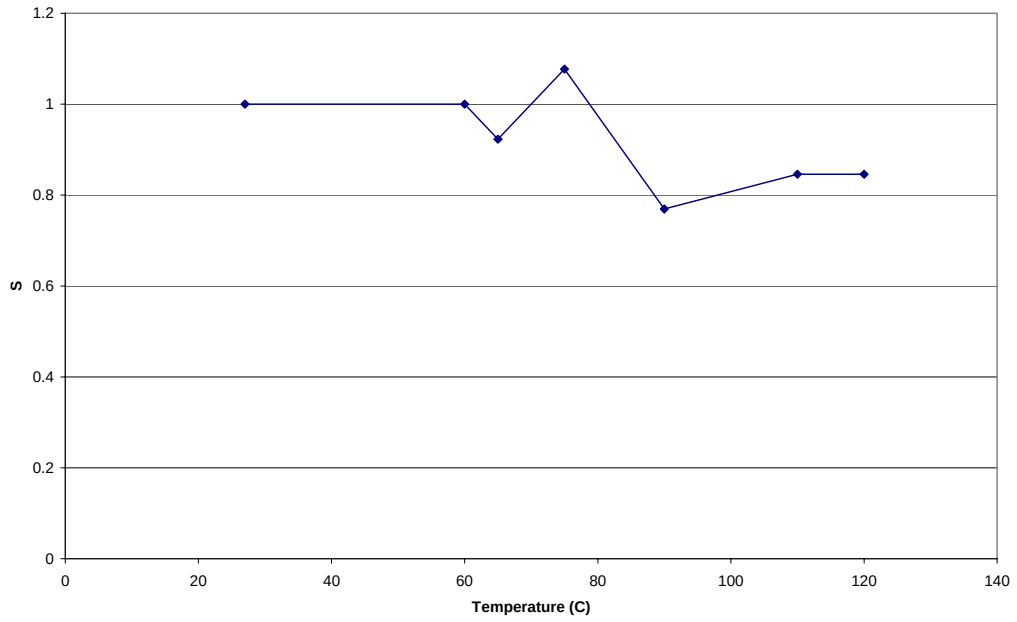

Figure 1.9: Saturation as a function of temperature.

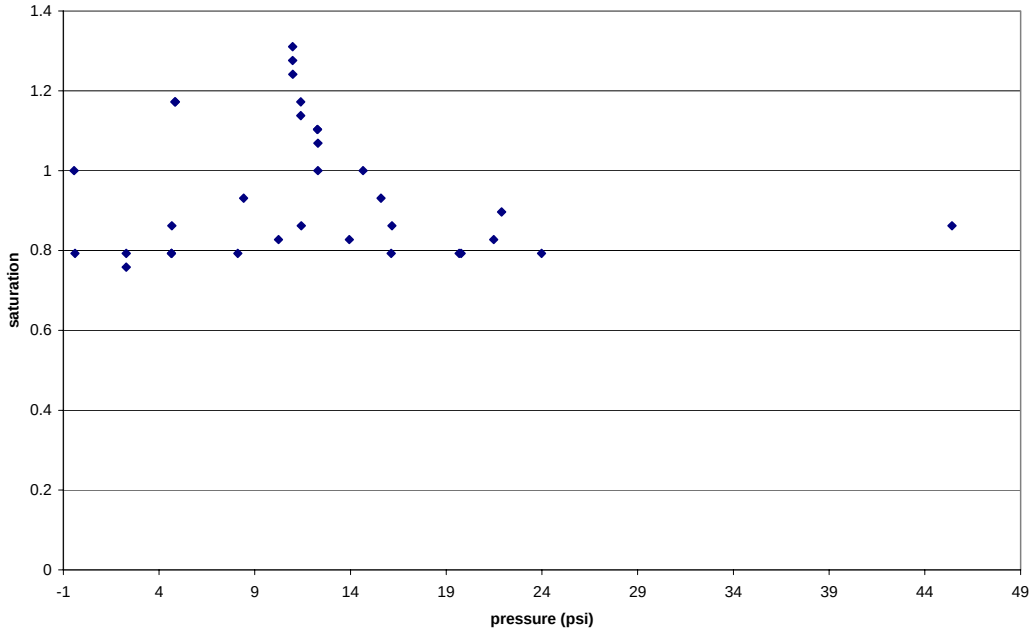

Figure 1.10: Saturation as a function of pressure.

1.2.3 Analyzing CT values using FP Image Viewer

It is possible to analyze the CT images using the software FP image viewer. Through script files, it is possible to process images. We modified the script files prepared by Dr. Serhat Akin to fit our purposes. In Figure 1.11 we show the input dry and wet files and the resulting porosity distribution. In this calculation we assumed CT_{air} = -1000 and CT_{water} =

0. Note that, using average CT values within the core, we found the average porosity to be 0.025. Using FP Image Viewer, we recognize that there is quite a variation in the porosity within the core. Figure 1.12 shows the plot of a cross section through the horizontal axis of the elliptical area of the core. This plot shows the variation of the porosity within the core. In Figure 1.11 we also notice artifacts of X-ray beam hardening effect, which were apparently absent in the original CT images. This suggests that if we use just the average CT values to analyze data, important information may be lost. Since the processing that could be done using script files is limited (or rather inconvenient), our plan is to transfer the CT value arrays to the MATLAB environment as a matrix, where they can be analyzed using the various matrix functions and graphical capabilities of this program. This will hopefully give us some more understanding as to why the results were different than the previous study. Also, we will understand whether the settings of the CT tool and/or the orientation of the sample holder need to be modified to achieve better images.

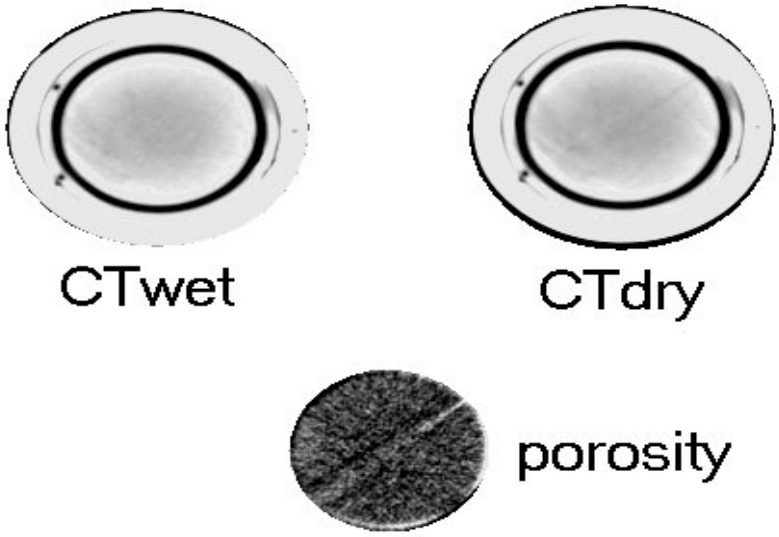

Figure 1.11: Calculation of the porosity distribution using FP Image Viewer. The 45° sloping line is due to beam hardening effect. The average porosity is 0.025, but it varies throughout the cross section of the core.

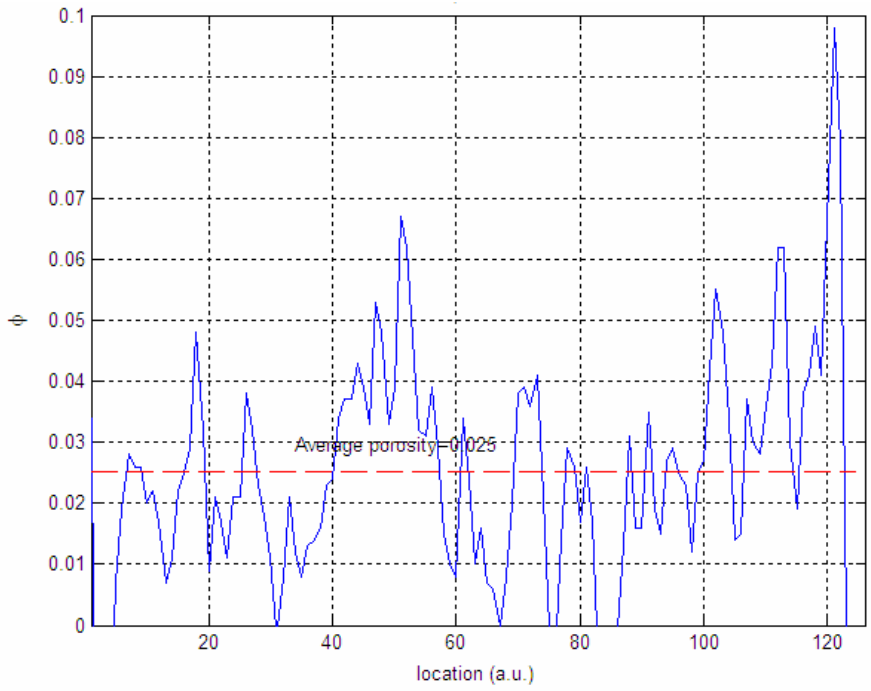

Figure 1.12: Variation of porosity across a horizontal cross section of the previous figure. The peak around the location 50 is due to the beam hardening effect.

1.3 CONCLUSIONS

For The Geysers rock sample, we made a pressure blowdown test and obtained CT measurements from a cross section of the sample as the pressure decreased. These data were used to calculate the saturation as a function of pressure. We found that it is very important to wait sufficiently so that the pressure stabilizes, sometimes up to 48 hours. We also found it useful to plot the pressure as a function of time and see the tendency to decide on the stabilization issue.

Since the experiment took almost a month, with the sample at 120 °C, it was important to monitor the apparatus all the time. For that we used a webcam and configured the computer that logs the data to be used remotely. That let us see the logged pressure and temperature any time from any location.

The experimental results we obtained are not conclusive, although we are still working on the CT images and analyzing them using different computer software. The graphs presented here are based on average CT values within the core. We noticed that the use of average CT values could be misleading as the heterogeneity within the sample is quite high. We are now working on the data to find a meaningful way of finding the saturation. The lack of clarity in the data, we believe, may be a consequence of insufficient energy levels in the CT scanner and some alignment problems. Although we thought we avoided

beam hardening by placing the core holder at an angle, a closer look at the results still reveals that this effect could not be avoided completely.

The next step is to analyze the data using more involved techniques, such as using MATLAB to deduce the parameters. The idea is to find regions of the data not affected by beam hardening and use those portions to calculate the local saturation. If we cannot achieve meaningful results from the analysis of the data, it will be necessary to repeat the experiment with The Geysers rock, before switching to a new rock sample; this time modifying CT scanner settings and the orientation and insulation of the apparatus to avoid X-ray beam hardening effect as much as possible.

2. INFERRING CAPILLARY PRESSURE FROM RESISTIVITY DATA

This research project is being conducted by Senior Research Engineer Kewen Li. The objective is to develop an approach to infer capillary pressure from resistivity data.

2.1 SUMMARY

A model has been derived theoretically to correlate capillary pressure and resistivity index. The model is simple and predicts a straight line relationship between capillary pressure and resistivity index on a log-log plot. To verify the model, gas-water capillary pressure and resistivity were measured simultaneously at room temperature in 14 core samples from two formations. The permeability of the core samples ranged from 0.028 to over 3000 md. The porosity ranged from less than 8% to over 30%. Capillary pressure curves were measured using a semipermeable porous-plate technique. The model was tested against the experimental data. The results demonstrated that the model could match the experimental data satisfactorily, demonstrating that capillary pressure can be inferred from resistivity data, using the model. An existing model was also tested against the experimental data. The results showed that the existing model did not work in most of the cases studied. The new model developed in this study will be useful to evaluate capillary pressure from resistivity data both in the laboratory as well as in actual reservoirs, especially in cases in which permeability is low.

2.2 INTRODUCTION

Both capillary pressure and resistivity index are important parameters in reservoir engineering. It is easier to measure resistivity index than capillary pressure in the laboratory, especially for core samples with low permeabilities. Resistivity logs can be run in a well, even in real time, but it is not possible to do this for capillary pressure. It would be useful if a relationship between capillary pressure and resistivity can be found, so that the easier measurement could substitute for the more difficult.

Resistivity, capillary pressure, and relative permeability have some similar features. For example, all are functions of fluid saturation and are influenced by pore structure and heterogeneity. Li and Horne (2005) derived a model to infer relative permeability from resistivity index. We speculated that capillary pressure may also be derived from resistivity index.

Szabo (1974) proposed a linear model to correlate capillary pressure with resistivity by assuming the exponent of the relationship between capillary pressure and water saturation is equal to that of the relationship between resistivity and water saturation. This assumption may not be reasonable in many cases. The linear model proposed by Szabo (1974) can be expressed as follows:

$$\frac{R_t}{R_0} = a + bP_c \tag{2.1}$$

where R_o is the resistivity at a water saturation of 100%, R_t is the resistivity at a specific water saturation of S_w, P_c is the capillary pressure, a and b are two constants.

The results from Szabo (1974) demonstrated that a single straight line, as predicted by the model (Eq. 2.1), could not be obtained for the relationship between capillary pressure and resistivity index.

Longeron *et al*. (1989) measured the resistivity index and capillary pressure under reservoir conditions simultaneously. Longeron *et al*. (1989) did not attempt to correlate the two parameters.

Literature on the relationship between capillary pressure and resistivity index has been infrequent. In this study, a theoretical relationship between capillary pressure and resistivity index was derived. In order to verify the relationship, gas-water capillary pressure and resistivity were measured simultaneously at room temperature using a semiporous-plate approach. In total, 14 core samples were tested.

2.3 THEORY

A theoretical relationship between capillary pressure and resistivity index is derived in this section. The basic idea behind this is that both capillary pressure and resistivity index are functions of the wetting phase saturation and the functions can be known from fractal modeling.

Toledo *et al.* (1994) reported that resistivity obeys a scaling law at low wetting phase saturations:

$$\frac{1}{R_t} \propto (S_w)^{\frac{1}{\beta(3-D_f)}} \tag{2.2}$$

where β is the exponent in the relation of disjoining pressures and film thickness, S_w is the wetting phase saturation, and D_f is the fractal dimension of the surface between the pore space and grains or matrix.

Toledo *et al.* (1994) also reported that capillary pressure follows another scaling law at low wetting phase saturations:

$$S_w \propto (P_c)^{-(3-D_f)} \tag{2.3}$$

Combining Eqs. 2.2 and 3, one can obtain:

$$P_c \propto (R_t)^{\beta} \tag{2.4}$$

It is known that R_t is equal to R_o when P_c is equal to p_e at a water saturation of 100%, which can be expressed as follows using Eq. 2.4:

$$p_e \propto (R_0)^{\beta} \tag{2.5}$$

Combining Eqs. 2.4 and 5:

$$P_c = p_e(\frac{R_t}{R_0})^{\beta} \tag{2.6}$$

Using the dimensionless form, Eq. 2.6 can be expressed as follows:

$$P_{cD} = (I)^{\beta} \tag{2.7}$$

where P_{cD} is the dimensionless capillary pressure (P_c/p_e); I is the resistivity index and, as a function of the wetting phase saturation, can be represented using the Archie's equation (1942):

$$I = \frac{R_t}{R_0} = S_w^{-n} \tag{2.8}$$

here n is the saturation exponent. R_0 depends on the porosity of a porous medium and can be calculated:

$$F_R = \frac{R_0}{R_w} = \phi^{-m} \tag{2.9}$$

where R_w is the resistivity of water, m is the cementation exponent, and F_R the formation factor.

According to Eq. 2.7, capillary pressure can be inferred from resistivity log data once the value of β is knows. This may provide a new approach to obtain capillary pressure data for reservoir engineering, using only measurements from well logs.

2.4 EXPERIMENTAL MEASUREMENTS

Experiments were conducted by CoreLab at room temperature to measure gas-water capillary pressure and resistivity simultaneously. The apparatus, and rock and fluid properties are described in this section.

Rock and Fluid Properties

The properties of the core samples used in this study are listed in Table 2.1. All the core samples were obtained from one oil reservoir. Group 1 core samples were from one formation with a high permeability and Group 2 samples were from another formation with a low permeability. The permeability in Group 1 ranged from 437 to 3680 md; the permeability in Group 2 ranged from 0.028 to 387 md.

Table 2.1: Properties of Core Sample

	Core No.	ϕ (f)	k (md)	ρ_g	F	S_{wr} (f)	m	n	R
Group 1	1	0.272	941	2.66	10.4	0.112	1.80	1.87	0.99
	3	0.281	1192	2.66	8.41	0.116	1.68	1.86	0.99
	6	0.191	999	2.65	15.5	0.134	1.65	1.82	0.91
	8	0.227	3680	2.65	11.8	0.067	1.67	2.00	0.98
	10	0.321	437	2.65	8.00	0.167	1.83	2.11	0.96
	16	0.262	1916	2.66	9.27	0.078	1.66	1.97	0.95
Group 2	152	0.114	1.49	2.63	122.3	0.519	2.21	2.49	0.92
	153	0.077	0.028	2.64	380.9	0.796	2.32	2.39	0.98
	204	0.179	0.560	2.69	43.9	0.617	2.20	1.82	0.92
	299	0.185	4.63	2.66	40.4	0.446	2.19	2.13	0.98
	334	0.234	387.	2.65	18.5	0.222	2.00	2.02	0.98
	336	0.163	35.3	2.66	40.1	0.388	2.03	2.23	0.95
	418	0.211	74.0	2.70	26.0	0.454	2.09	2.26	0.99
	479	0.210	28.3	2.68	29.9	0.560	2.18	1.91	0.98

The brine used for Group 1 core samples had a salinity of 90,000 ppm with a resistivity of 0.078 ohm-m at 25°C. The brine used for Group 2 core samples had a salinity of 20,000 ppm with a resistivity of 0.308 ohm-m at 25°C.

Apparatus

A schematic of the apparatus used for the combined measurements of gas-water capillary pressure and resistivity is shown in Figure 2.1. The outside of each porous plate was painted with silver paint. The resistivity meter was manufactured by Quad Tech and the model was 1730 LCR. The frequency used in this study was 20,000 Hz.

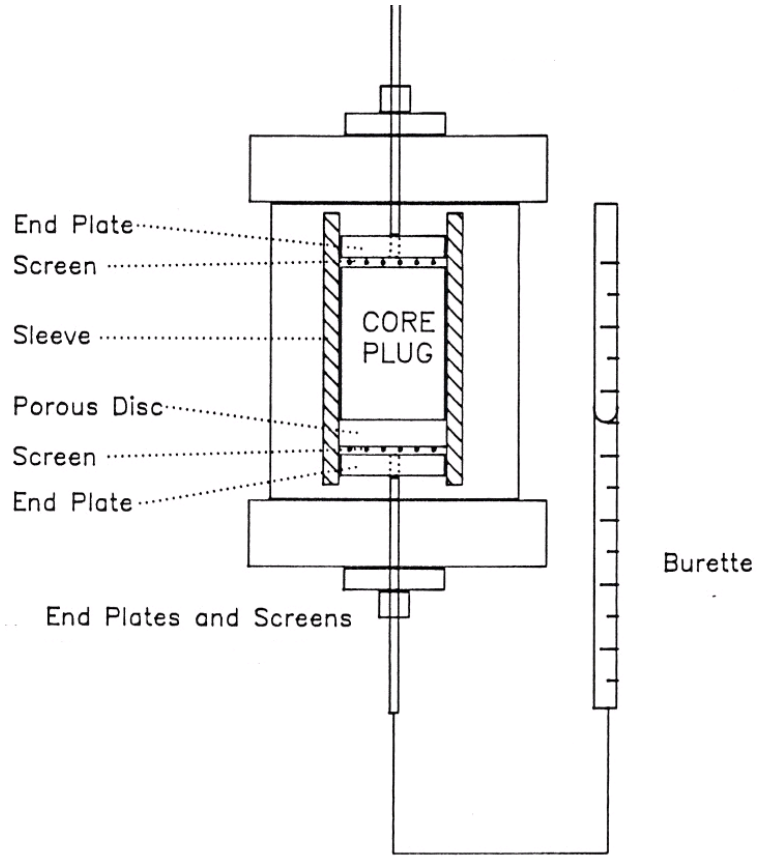

Figure 2.1: Schematic of experimental apparatus for measuring capillary pressure.

Experimental Procedure

The samples designated for these analyses were cleaned and dried prior to testing. Permeability and porosity were measured after cleaning. Then the samples were evacuated and saturated with synthetic formation brine. After loading the sample and the porous plate into the core holder at an appropriate net stress, brine was flushed using a 500 psi back pressure to ensure a complete saturation. Resistivity was measured, followed by injection of several pore volumes of brine. The resistivity at a water saturation of 100% was measured again the following day until stabilized (less than 1% change per day). Formation resistivity factor (FRF) at stress was determined at this point.

The sample was desaturated beginning at a low pressure by injecting humidified air at a regulated capillary pressure. The volume and weight of displaced brine were monitored and used to calculate the brine saturation. Resistivity, capillary pressure, and brine saturation were measured daily at each pressure point until saturation was stabilized (less than 1% change per day). This was repeated until no water was produced.

At the end of the test, each sample was removed and its weight was measured. The Dean-Stark method was used to extract water, methanol soxhlet method was used to extract salts, and the sample was dried to a constant weight in a vacuum oven at 100°C. The final

dry weight was measured. Dean-Stark water extracted was used to confirm the final water saturation.

2.5 RESULTS

The experimental data of capillary pressure and resistivity index in core samples from two formations were used to test the model (Eq. 2.6) proposed in this study. The results are presented and discussed in this section.

Figure 2.2 shows the relationship between formation factor and porosity for all the samples from two formations. The values of cement exponent were calculated using Eq. 2.9: *m* is equal to 1.71 for the core samples in Group 1 (formation 1) and is equal to 2.19 for core samples in Group 2 (formation 2).

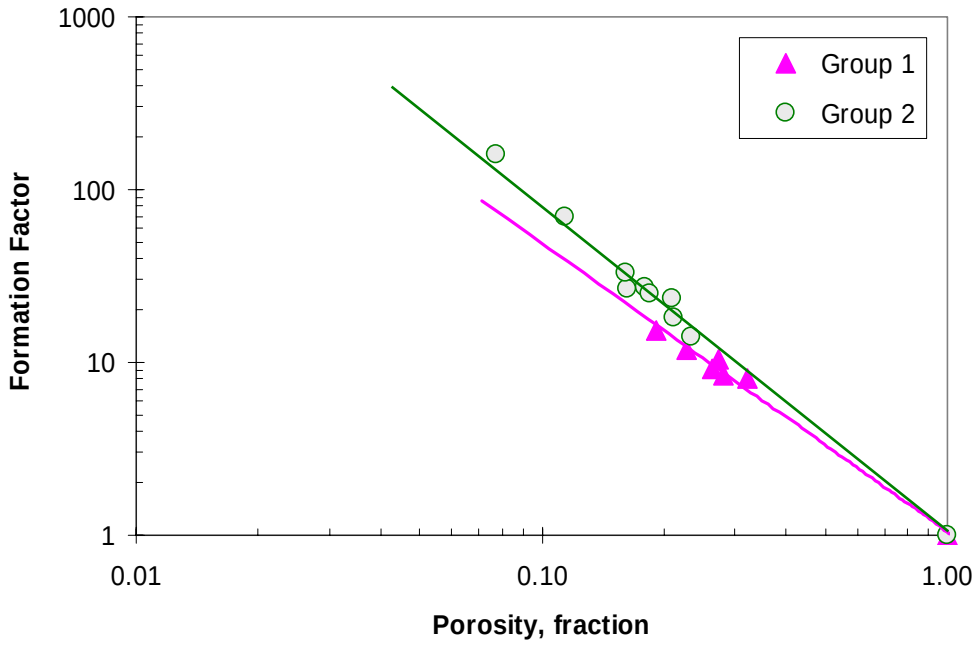

Figure 2.2: Relationship between formation factor and porosity for all the samples from two formations.

The data of resistivity index vs. water saturation for the core samples in Group 1 (high permeability) are shown in Figure 2.3. The data points follow Archie's equation (Eq. 2.8). The values of saturation exponent were calculated for each core sample using Eq. 2.8 and the results are shown in Table 2.1. The value of *n* ranges from 1.82 to 2.11 and the average value is about 1.94. The average value was calculated by conducting regression analysis for all of the data points.

For the low permeability formation (Group 2), the experimental data of resistivity index are shown in Figure 2.4. The values of saturation exponent calculated using Eq. 2.8 are also listed in Table 2.1. The value of *n* ranges from 1.82 to 2.49 and the average value is about 2.13.

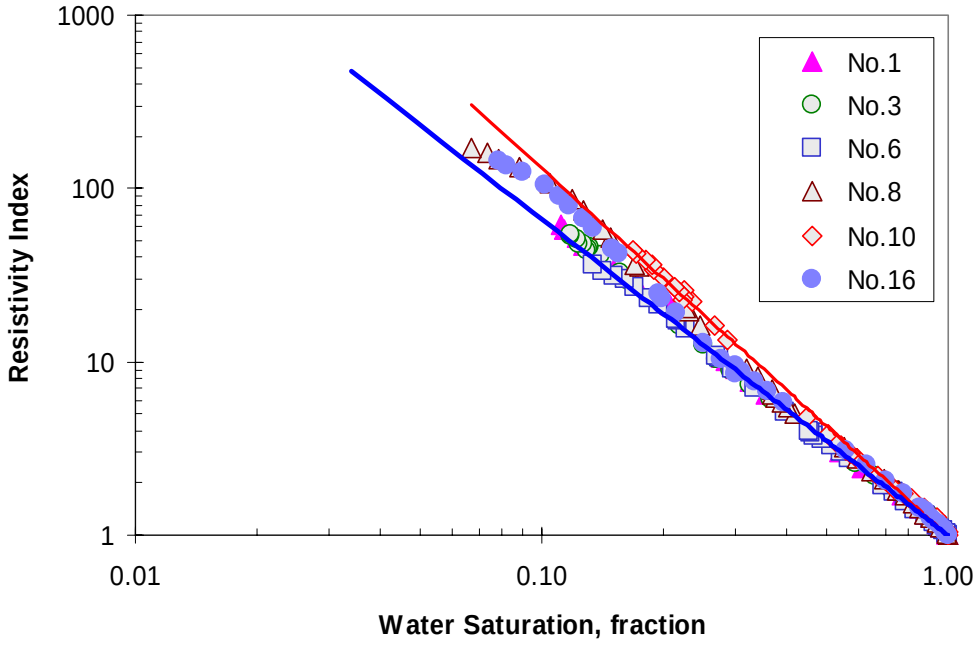

Figure 2.3: Relationship between resistivity index and water saturation for the samples in Group 1.

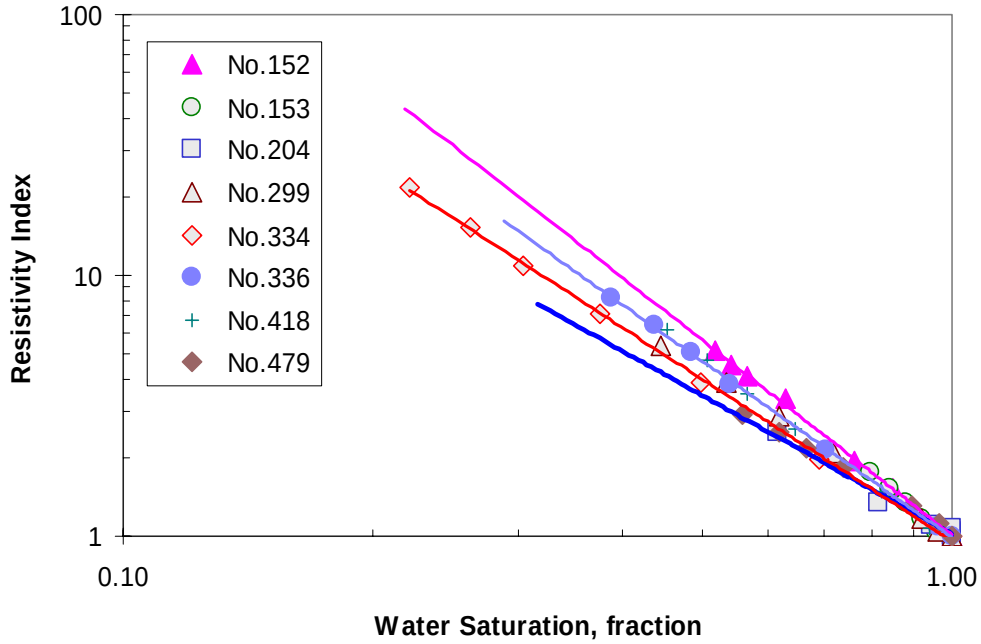

Figure 2.4: Relationship between resistivity index and water saturation for the samples in Group 2.

It is necessary to have the experimental data of capillary pressure to verify the model represented by Eq. 2.6. The capillary pressure data of the core samples in Group 1 are shown in Figure 2.5 and those of Group 2 are shown in Figure 2.6. According to Eq. 2.3, the relationship between capillary pressure and water saturation is linear in the range of small water saturation. Figs. 2.5 and 6 show such a feature. Note that the range of water saturation in which the linear relationship exists is very narrow for the No.3 core sample (see Figure 2.5). One can see from Figs. 2.5 and 2.6 that the range of water saturation in which the linear relationship exists depends upon permeability. For the core samples with a low permeability, the straight line crosses over almost the entire range of water saturation from 1 to S_{wr} (residual water saturation). For the core samples with a high permeability, however, the straight line crosses over only the part with small water saturation.

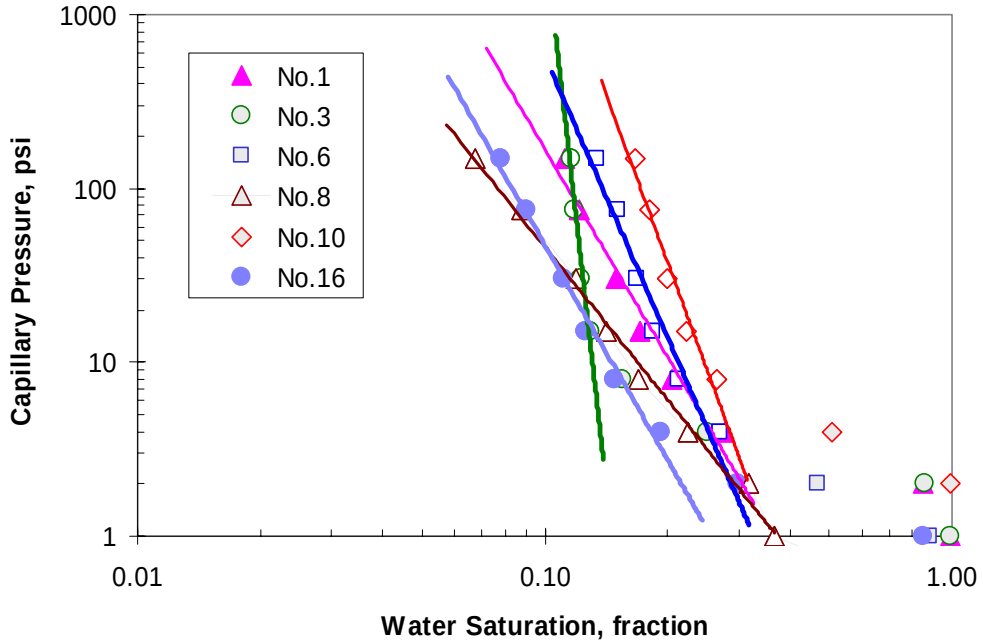

Figure 2.5: Capillary pressure curves of the samples in Group 1 (high permeability).

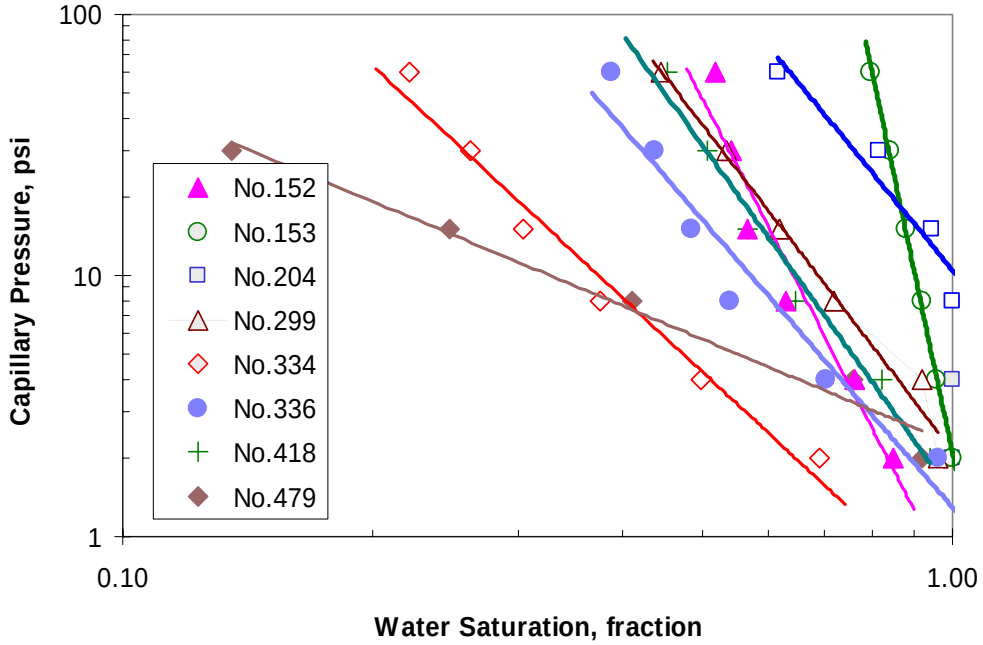

Figure 2.6: Capillary pressure curves of the samples in Group 2 (low permeability).

The relationships between capillary pressure and resistivity index of Groups 1 and 2 are shown in Figs. 2.7 and 2.8 respectively. In Figure 2.7, a straight line exists in the range with larger capillary pressure and resistivity index (corresponding to small water saturation), as predicted by the model (Eq. 2.6) derived in this study.

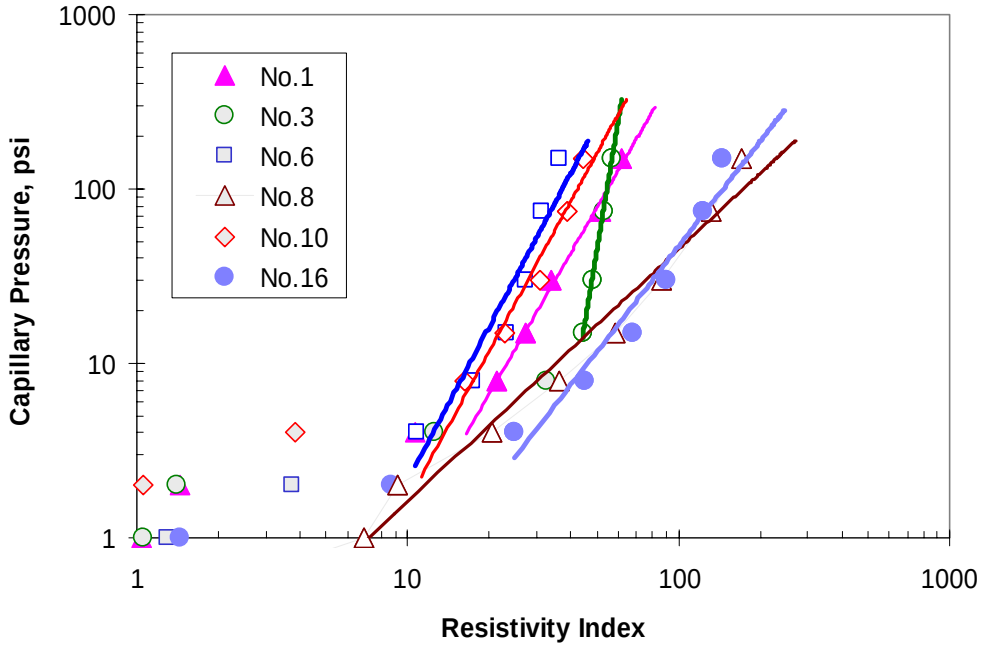

Figure 2.7: Relationship between capillary pressure and resistivity index of Group 1 (high permeability).

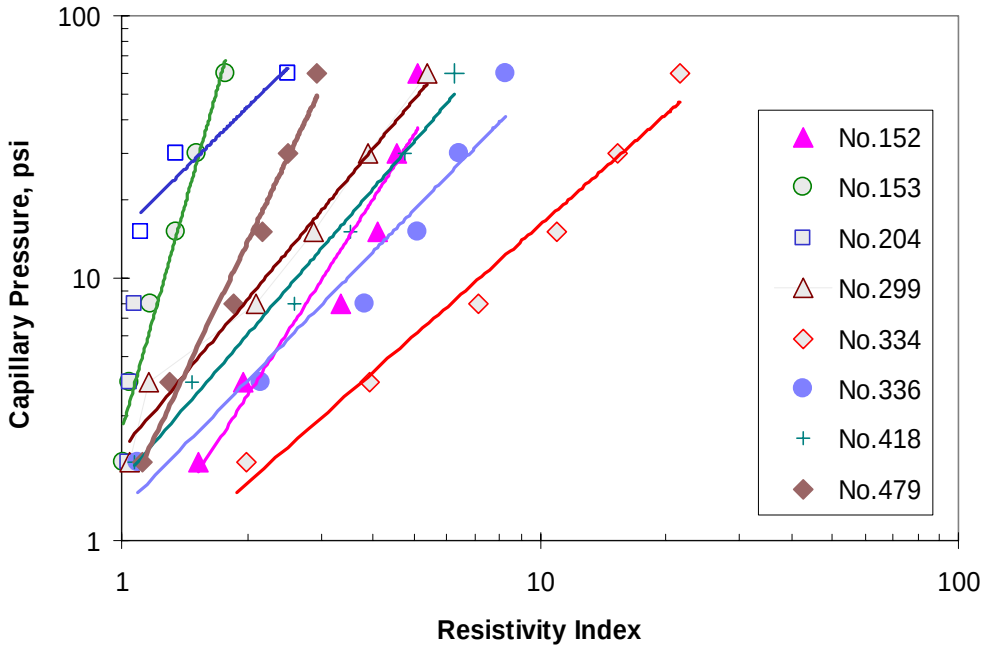

Figure 2.8: Relationship between capillary pressure and resistivity index of Group 2 (low permeability).

Interestingly, a straight line exists for almost all of the data points in the core samples with low permeability (see Figure 2.8). This demonstrates that the model (Eq. 2.6) derived from fractal modeling works satisfactorily.

The values of regression coefficient (R), i.e., the goodness of fitting of the model to the data shown in Figs. 2.7 and 2.8, were calculated and are listed in Table 2.1. One can see that the goodness of fit is satisfactory.

As stated previously, Szabo (1974) proposed a linear model (Eq. 2.1) to correlate capillary pressure and resistivity by assuming the exponent of capillary pressure curve is equal to that of the resistivity index curve. To test this model, the experimental data in Figs. 2.7 and 2.8 are plotted in Figs. 2.9 and 2.10 using a linear scale instead of a logarithmic scale. Comparing the results shown in Figs. 2.7 and 2.8 to those plotted in Figs. 2.9 and 2.10, one can see clearly that the model (Eq. 2.6) derived in this study has a better fit to the experimental data than the linear model (Eq. 2.1) in the cases studied.

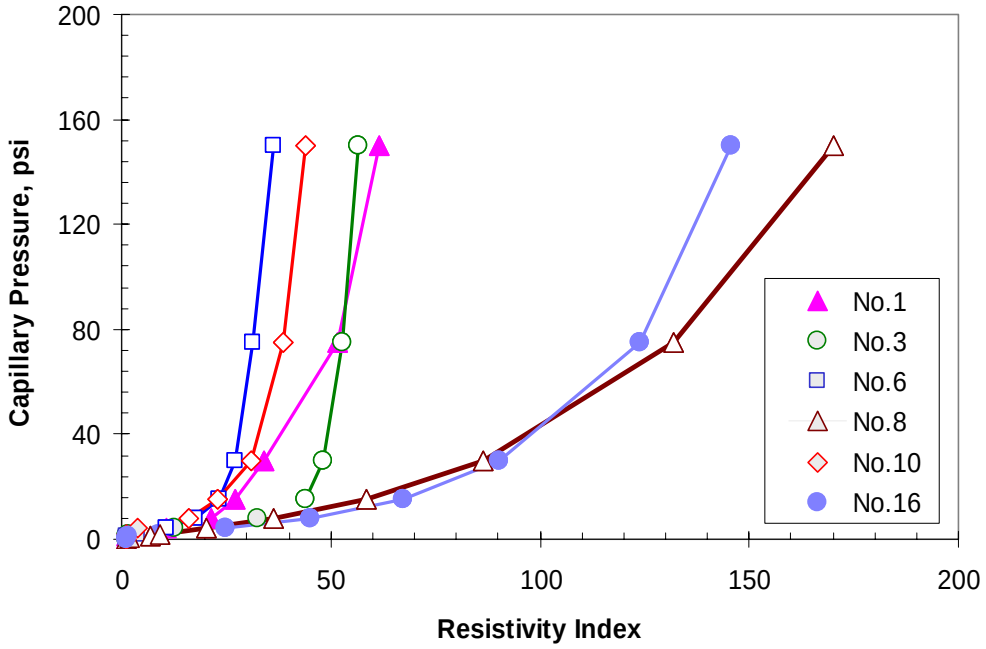

Figure 2.9: Relationship between capillary pressure and resistivity index of Group 1 (high permeability) in a linear coordinate plot.

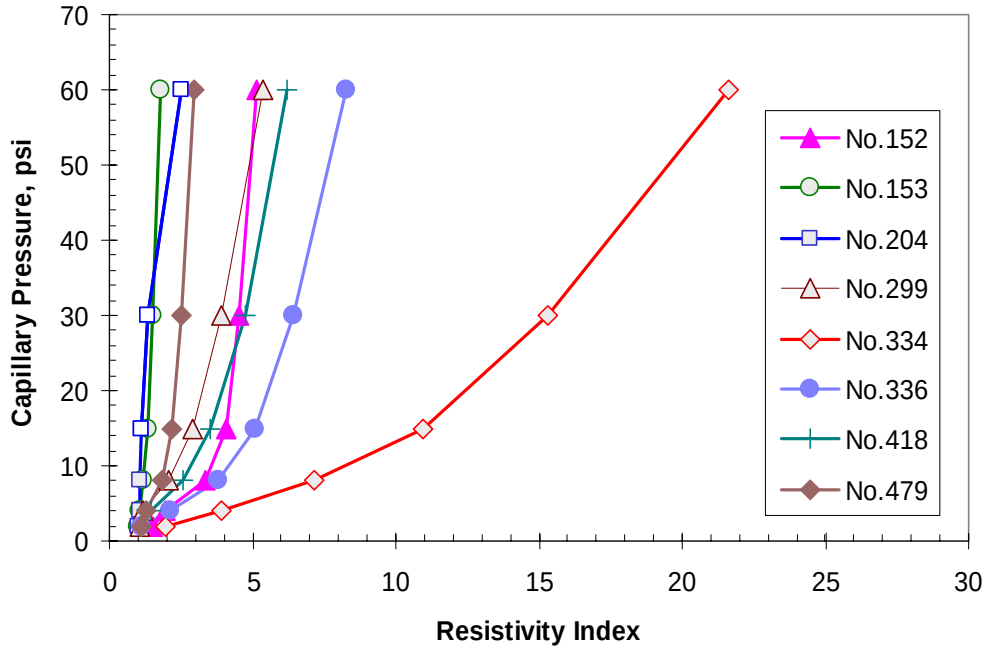

Figure 2.10: Relationship between capillary pressure and resistivity index of Group 2 (low permeability in a linear coordinate plot).

The values of β were calculated using Eq. 2.6 with the data shown in Figs. 2.7 and 2.8. For most of the core samples, the value of β is in the range from 1 to 3. The effect of permeability on β for the core samples in both Group 1 and 2 is shown in Figs. 2.11 and 2.12 respectively.

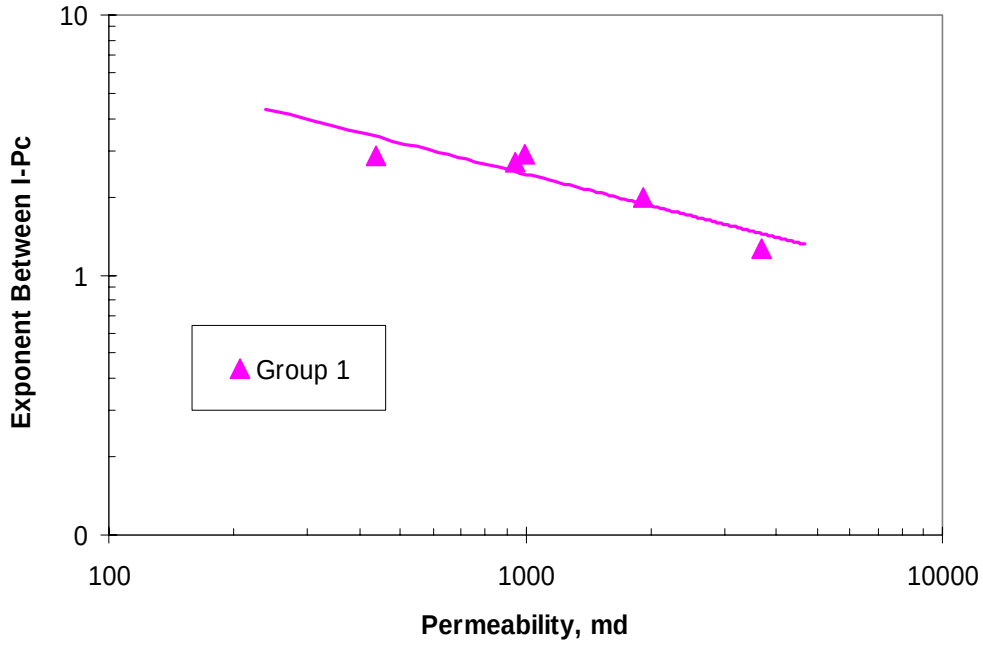

Figure 2.11: Effect of permeability on β for the core samples in Group 1 (high permeability).

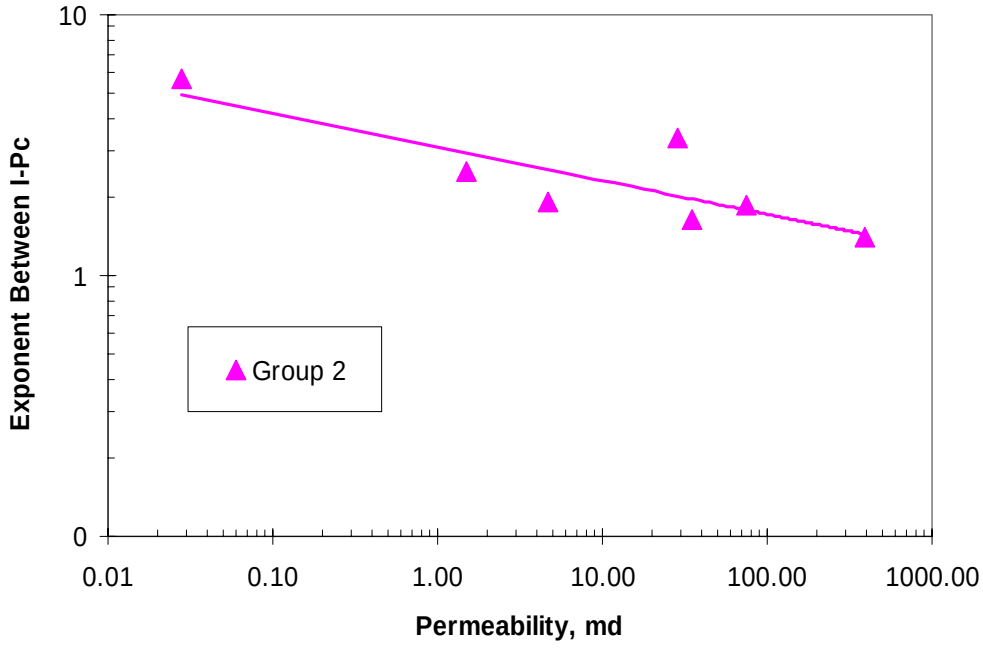

Figure 2.12: Effect of permeability on β for the core samples in Group 2 (low permeability).

In the cases studied, for both Group 1 and 2, the value of β decreases with the increase in permeability. The relationship between permeability and β is linear in a log-log plot, as shown in Figs. 2.11 and 2.12. The values of correlation coefficient for Group 1and 2 are 0.82 and 0.71 respectively.

2.6 CONCLUSIONS

Based on the present work, the following conclusions may be drawn:

1. A model was developed theoretically to correlate capillary pressure and resistivity index. This model predicts a power law relationship between capillary pressure and resistivity index.
2. The model derived in this study was tested against experimental data in 14 core samples. The permeability ranged from 0.028 to over 3000 md. The results demonstrated that the model works satisfactorily.
3. The model works better in core samples with low permeabilities than in those with high permeabilities.
4. The experimental results showed that the relationship between capillary pressure and resistivity index is not linear, as the previous model proposed.
5. The value of β decreases with the increase in permeability. The relationship between permeability and β is linear in a log-log plot in the cases studied.

3. DOWNHOLE ENTHALPY MEASUREMENT

This research project is being conducted by Research Assistant Egill Juliusson, Senior Research Engineer Kewen Li and Professor Roland Horne. The objective of this project is to find a way to measure enthalpy downhole either by constructing a device specifically for that purpose or expanding the use of existing measurement technologies.

3.1 SUMMARY

This report describes data analysis methods that have been used to extract information from measurements of segmented air-water bubble flow. The discussion is divided into two sections; one describes a method to measure bubble velocity from the signals obtained from the resistivity and phototransistor sensors described in the Quarterly Report from Spring 2005. The other describes two approaches to infer the void fraction from the given data. These two approaches have not shown satisfactory results but a fundamental understanding of the problems involved has been gained from the analysis.

The sensor and experiment design needs to be improved to achieve a more reliable way to estimate the void fraction. Future work will also include moving over to tests in a 4 inch diameter plexiglass tube.

3.2 DATA ANALYSIS

3.2.1 Bubble velocity

In order to calculate the enthalpy rate in two-phase flow, the steam and liquid average velocities need to be determined. A part of this is to find the velocity of the steam bubble as it travels up the borehole. Using the signals obtained from two sensors, spaced a known distance apart, this bubble velocity can be inferred. Given the distance between the sensors, L, the mean bubble velocity will be

$$v = \frac{L}{t_t} \qquad .(3.1)$$

We only need to find the time, t_t, it takes the bubble to travel from one sensor to the other, i.e. the time shift between the patterns measured by each sensor. For slow and dispersed bubble flow (Figure 3.1) this can easily be seen from a quick look at the signals but when the bubble flow becomes more rapid (Figures 3.2 and 3.3) the pattern in the signal becomes harder to discern.

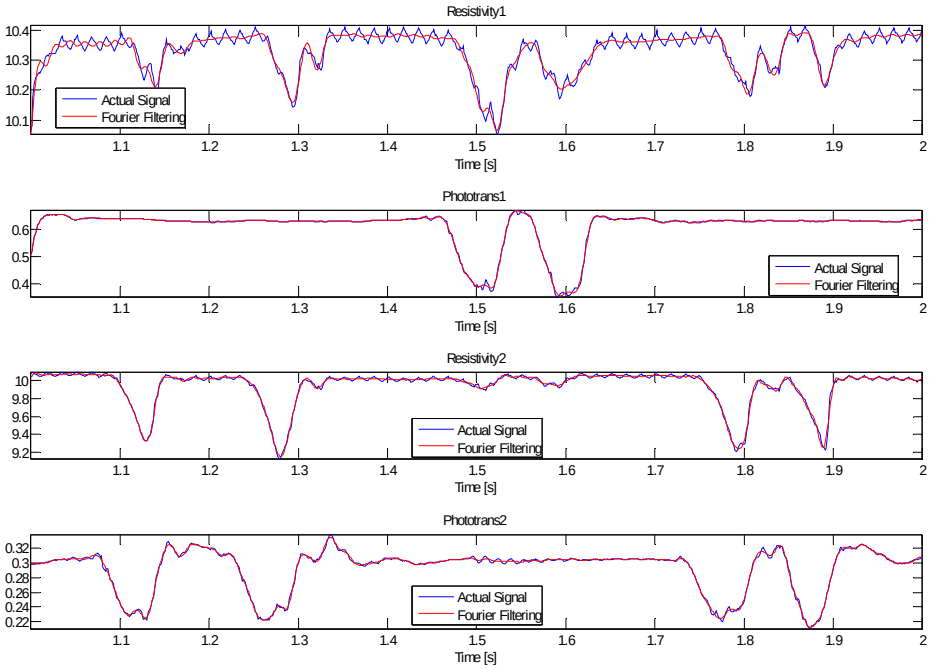

Figure 3.1: Signals obtained from two different types of sensors placed at two different locations (approximately 5 cm apart). The upper two measurements are taken at location 1 and the lower two are taken at location 2. The bubble flow was relatively slow and dispersed. Hence a bubble pattern is clearly detectable and the time shift can be estimated visually. This will be referred to as Pilot test 2.

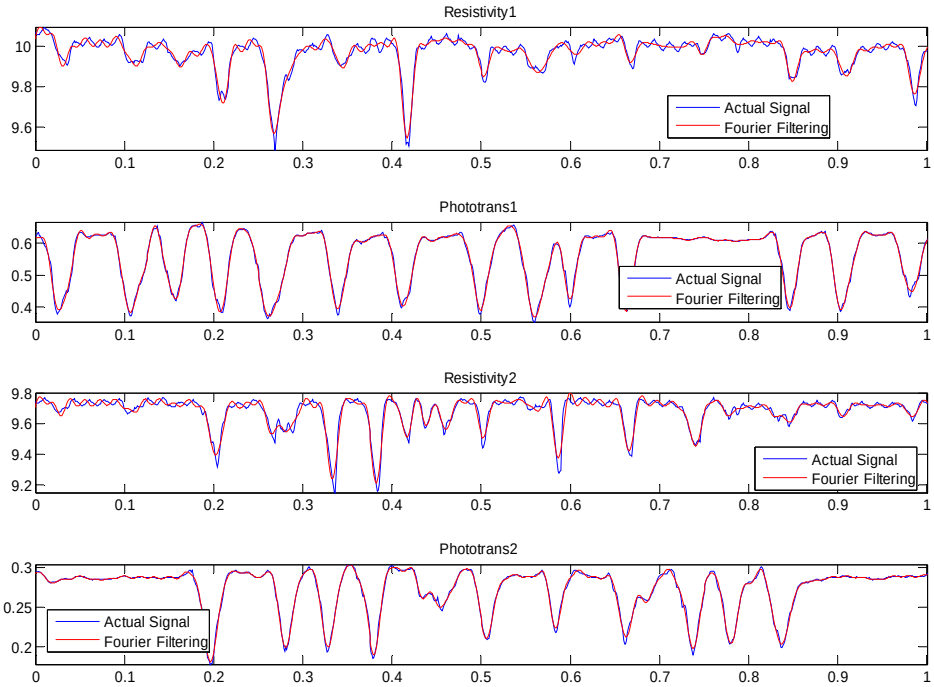

Figure 3.2: Signals from the resistivity and phototransistor sensors. As seen by comparison to the signals in Figure 3.1, the bubble flow is getting more rapid and the pattern is now harder to discern. This will be referred to as Pilot test 1.

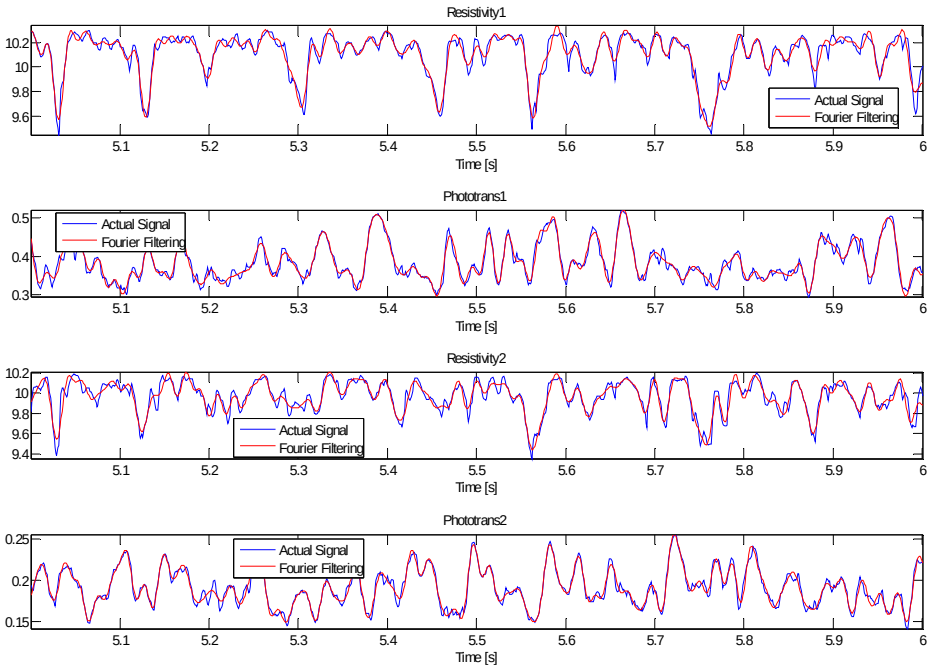

Figure 3.3: Here we see the response from the same sensors as in used previously but now the bubble flow is much more rapid. This makes the bubble pattern and hence the time shift very hard to discern. This will be referred to as Pilot test 3.

A relatively simple but robust method to find the time shift in the signals is to calculate the cross-correlation function (XCF) between the two signals. The cross-correlation function is a function of the correlation coefficient between the two signals, where one of the signals has been shifted in time. The time at which the XCF has its maximum value then corresponds to the time shift between the two signals. The XCF is defined as follows:

$$R_{xy}(\tau) = \frac{1}{t_{tot}} \int_0^{t_{tot}} (x(t-\tau) - \bar{x})(y(t) - \bar{y}) dt \tag{3.2}$$

Here x and y are the two signals, $\bar{x}$ and $\bar{y}$ are the signal averages over the entire measurement interval, t_{tot}, and τ is the time shift. This method is commonly used in flow metering technology and has worked well to measure concentration signals that are stochastic in nature. This is most often the case in turbulent two-phase flows. The method was tested on each of the signals and the results for Pilot test 2 and 3 are shown in Figures 3.4 and 3.5.

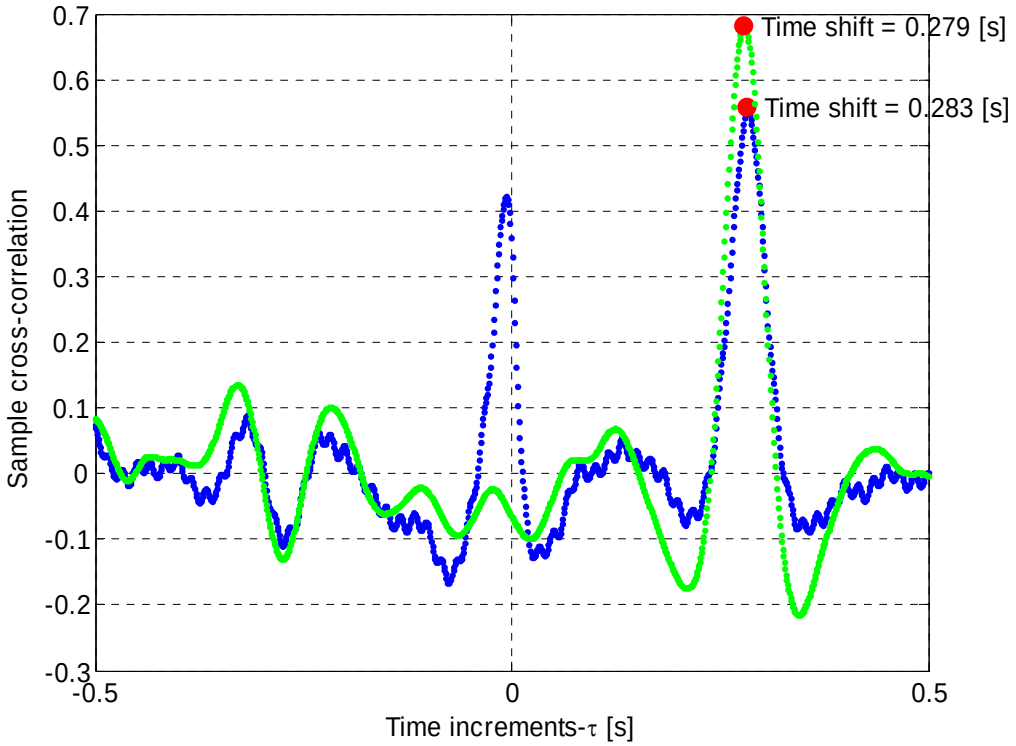

Figure 3.4: This graph of $R_{xy}(\tau)$ for each sensor type (test corresponding to Figure 3.1) shows a clear maximum at $\tau \approx 0.28$ s. Phototransistor data are in green and resistance data are in magenta. This is to verify that the cross correlation method works.

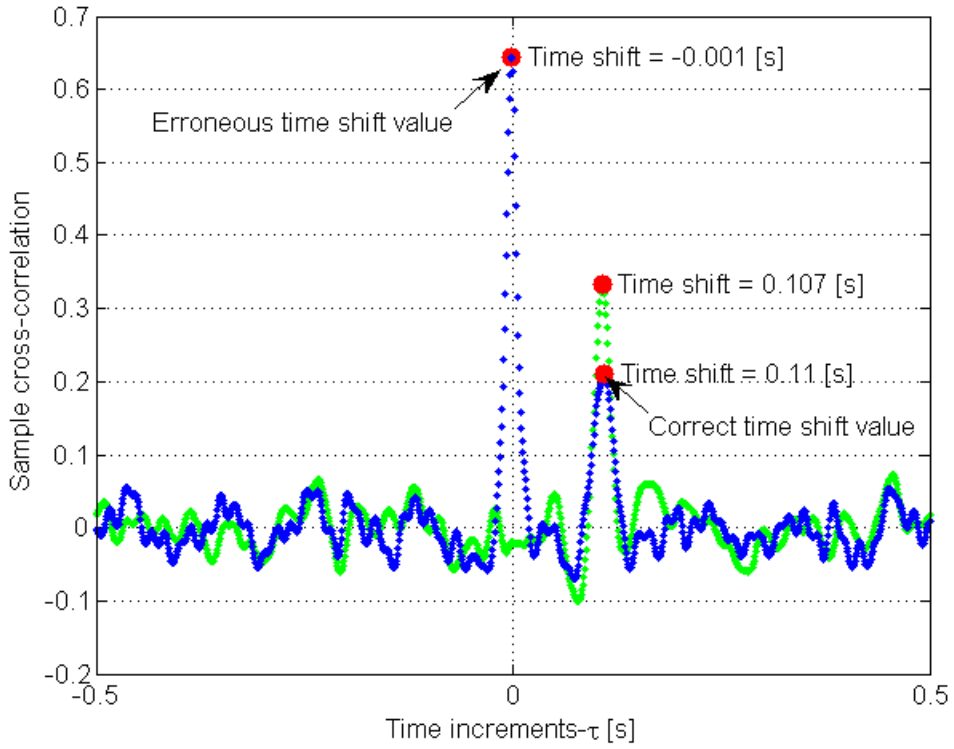

Figure 3.5: This graph of $R_{xy}(\tau)$ for each sensor type (test corresponding to Figure 3.3) shows a clear minimum at $\tau \approx 0.11$ s. The erroneous value of -0.001 s is predicted by the resistivity sensor because of crosstalk between the electrodes. This can however be fixed e.g. by subtracting the latter signal (y) from the first signal (x) and then cross correlating x-y and y. Other methods would be to apply a limit to the minimum value of τ or simply inspect the data manually.

As these figures show, the time shift can be found surprisingly clearly and accurately by this method. The only case in which the method brakes down, is when measuring the rapid bubble flow using the resistivity sensors. In that case the minimum difference is found when the time shift, $\tau \approx 0$. This erroneous result is introduced because of crosstalk between the two electrode sensors. The crosstalk effect is explained further in the Quarterly Report from Spring 2005. A way to fix this problem is discussed at the end of this section.

A second method to determine the time shift was also devised, and will be presented here to give comparison to the results obtained from the cross-correlation function. The basic idea is to find the time shift that gives the minimum difference when one signal is subtracted from the other. Since the signals are not necessarily at the same scale we must scale one of the signals by the ratio of the averages of the two signals, and then look at the difference. The time shift between the signals is the value that minimizes this quantity. More compactly we might say that we want to find τ subject to:

$$\min\left\{\Delta xy(\tau) = \left| x(t) - \frac{\bar{x}}{\bar{y}} y(t+\tau) \right|\right\} \tag{3.3}$$

Here x and y are the signals from each sensor as a function of time and the overbar denotes the signal average over the total measurement interval (just as defined previously). Since the data sets at hand are usually not very large it is easy to calculate the difference Δxy as a function of τ (using MATLAB or a similar numerical tool) on some reasonable interval and find the time shift corresponding to the minimum value in that dataset. Figures 3.6 and 3.7 show $\Delta xy(\tau)$, calculated from the signals in Pilot tests 1 and 3.

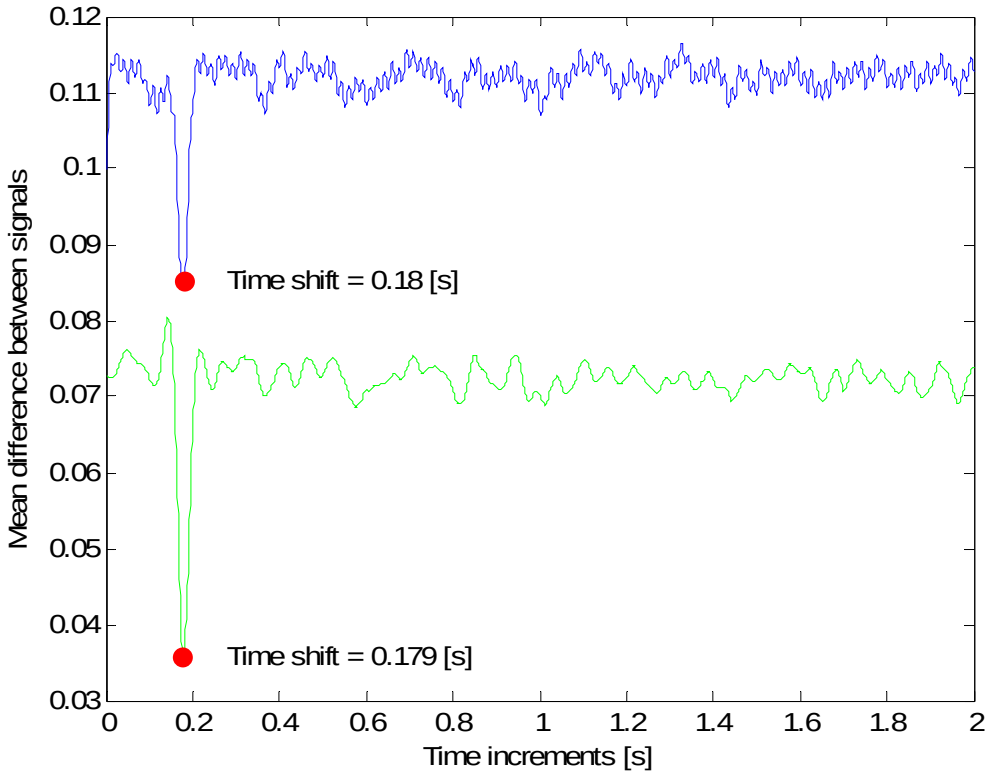

Figure 3.6: This graph of $\Delta xy(\tau)$ for each sensor type (test corresponding to Figure 3.2) shows a clear minimum at $\tau \approx 0.18$ s. Phototransistor data are in green and resisivity data are in blue. This shows that the time shift and hence the bubble velocity can be calculated using this relatively simple correlation method.

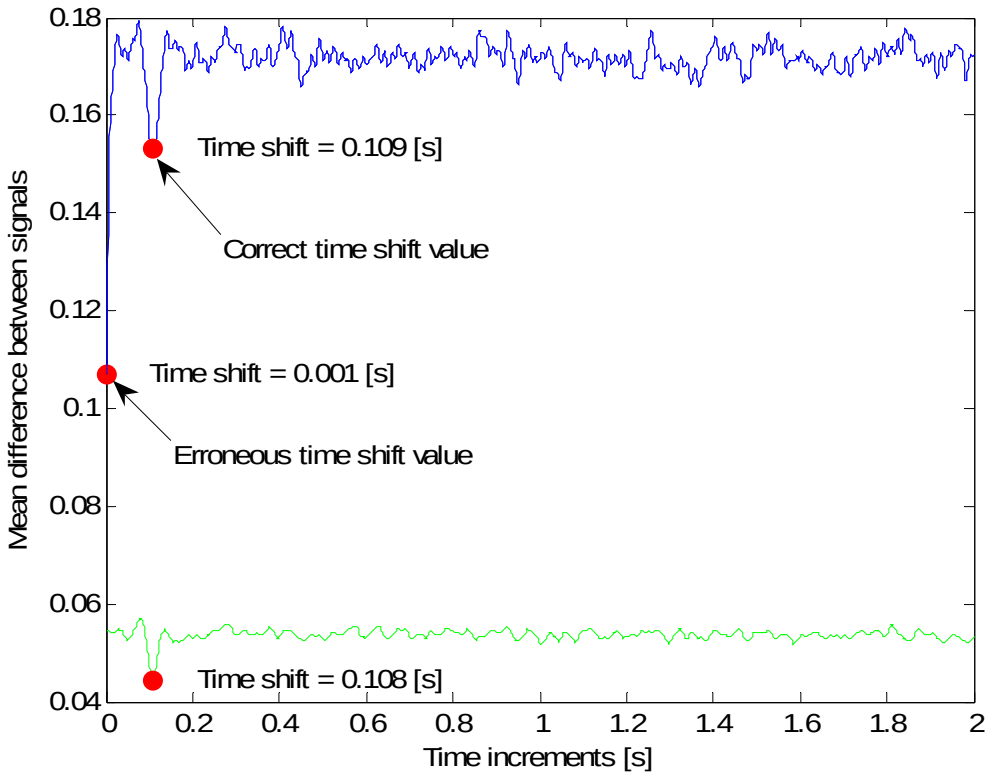

Figure 3.7: This graph of $\Delta xy(\tau)$ for each sensor type (test corresponding to Figure 3.3) shows a clear minimum at $\tau \approx 0.11$ s. The erroneous value of 0.001 s is again predicted by the resistivity sensor because of crosstalk between the electrodes.

As we see, the results of this method are very consistent with those from the cross-correlation technique. In these two cases it even seems that this method is more consistent, since the variability between the time shifts predicted by each sensor is smaller.

There are a few alternate ways to deal with the crosstalk in the resistivity measurements. The best way would of course be to eliminate or minimize the physical phenomena, but that would require the distance between the electrodes to be very large in comparison to the bubble sizes. Therefore we would expect more ambiguity in the cross correlations because the bubble geometries might have changed in the time it takes to travel between the sensors.

Another method would be to assume some minimum possible time shift, $\tau_{min}>0$, (e.g. based on an estimate of the maximum possible bubble velocity) and then find the maximum value of $R_{xy}(\tau)$ for $\tau>\tau_{min}$. The disadvantage of this method is obviously that an estimate of the maximum bubble velocity or τ_{min} is needed before the measurement has been made, and most researchers would want to manually inspect the data anyway to make sure their estimate was correct. This brings up the third option which would be to manually inspect the data and estimate τ_{min} without assuming anything beforehand. This

is almost equivalent to the second option and likewise could become cumbersome when dealing with a large number of measurements.

The fourth option, and this is the one recommended here, is to subtract the lagging signal (y) from the leading signal (x) and then cross correlate $z = x - y$ to y. This way we can subtract the erroneous part of the signal (resulting from crosstalk) out of the leading signal and the peak in $R_{xy}(\tau)$ at $\tau \approx 0$ will be eliminated. An example of this is shown in Figure 3.7

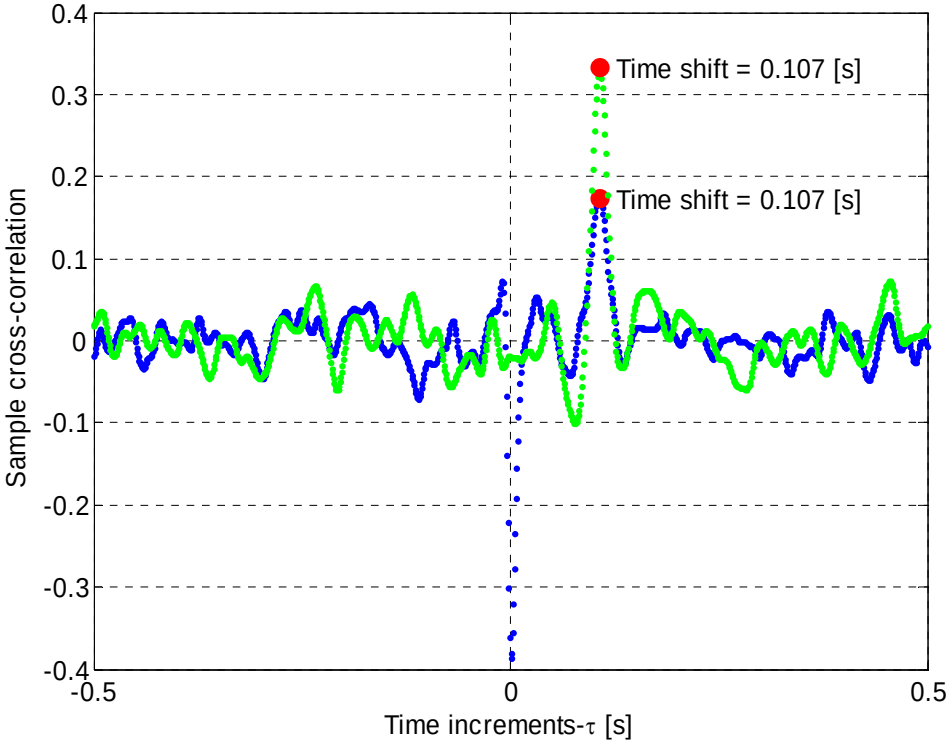

Figure 3.7: The cross-correlation between the lagging signal (y) and the difference between the leading and the lagging signal (z=x-y) provides an appropriate estimate of the time shift.

3.2.2 Void fraction and bubble geometry

One of the more important quantities that one would like to measure in downhole wellbore flow is the void fraction. To that end, estimating the bubble frequencies and being able to count the bubbles becomes important. This has proven to be nontrivial using the electrical resistivity measurements, due to the low signal-to-noise ratio. This section will introduce some of the problems involved and the methods that have been used for the analysis.

Since this experiment deals with segmented flow the bubble geometry can be estimated as a cylinder of diameter equal to the tubing diameter and length $L_{b,i}$ which can be calculated as:

$$L_{b,i} = vT_{b,i} \tag{3.4}$$

where v is the bubble velocity (as obtained in Section 3.2.1) and the $T_{b,i}$ is the time it takes bubble number i to pass the sensor. Another property that arises from the fact that the flow is segmented is that the water and air flow velocities will be the same, and therefore the void fraction, X, can be calculated as

$$X = \frac{V_{air}}{V_{tot}} = \frac{\sum_i AL_{b,i}}{AL_{tot}} = \frac{\sum_i L_{b,i}/v}{L_{tot}/v} = \frac{\sum_i T_{b.i}}{T_{tot}} \tag{3.5}$$

where V is the volume, A is the cross sectional area of the flow, L_{tot} is the total length of fluid (air and water) that has passed through the measured section and all other quantities are as defined earlier in this report. Hence we see that the void fraction is simply the total time that we have a signal corresponding to a bubble divided by the total measurement time.

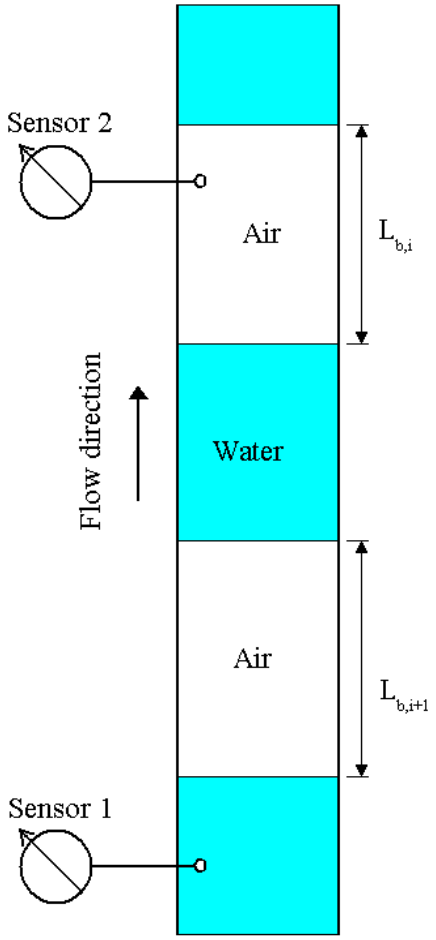

Figure 3.8: A simplified model of vertical segmented flow. By assuming that the water and air velocities are the same, the void fraction can be calculated as the ratio between the total time that the sensor measures the presence of air and the total measurement time.

Given these assumptions, the total time that bubbles are present is all that is needed to calculate the void fraction. But this quantity is not so easily determined from these measurements because of the relatively slow response time of the sensors. Moreover, in

the case of the resistivity measurements, the low signal-to-noise ratio and the crosstalk complicate the analysis even more. Two basic methods have been tried to infer consistent estimates of the void fraction between all four sensors without satisfactory results.

In the first method we make a histogram of the measurement points and try to find some intermediate value that could correspond to a transition value between air and water measurements. This intermediate value should be somewhere between the two peaks corresponding to measurement values for air and water as shown in Figure 3.9 (data taken from Pilot test 1).

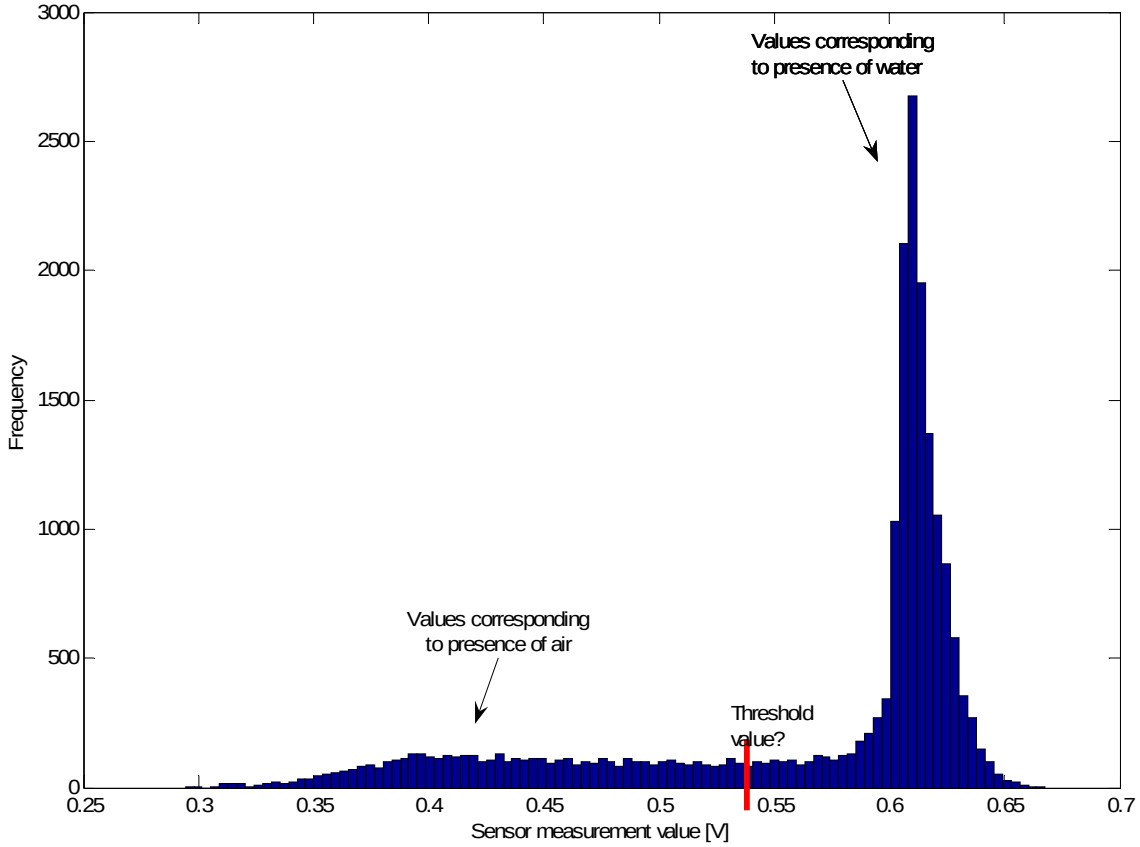

Figure 3.9: A histogram of measurements made with phototransistor 1 at an intermediate flow rate. An example of the actual signals is shown in Figure 3.2. As this figure shows it is not clear where the threshold value for transition between air and water measurements lies.

As seen in Figure 3.9 the threshold value for transition between air and water measurements is not clearly defined when looking at the histogram for the phototransistor measurements. The situation does not improve we look at the resistivity measurements as can be seen in Figure 3.10. Thus, we abandon this method for the time being, although it might become feasible if the time response and accuracy of the sensors could be improved.

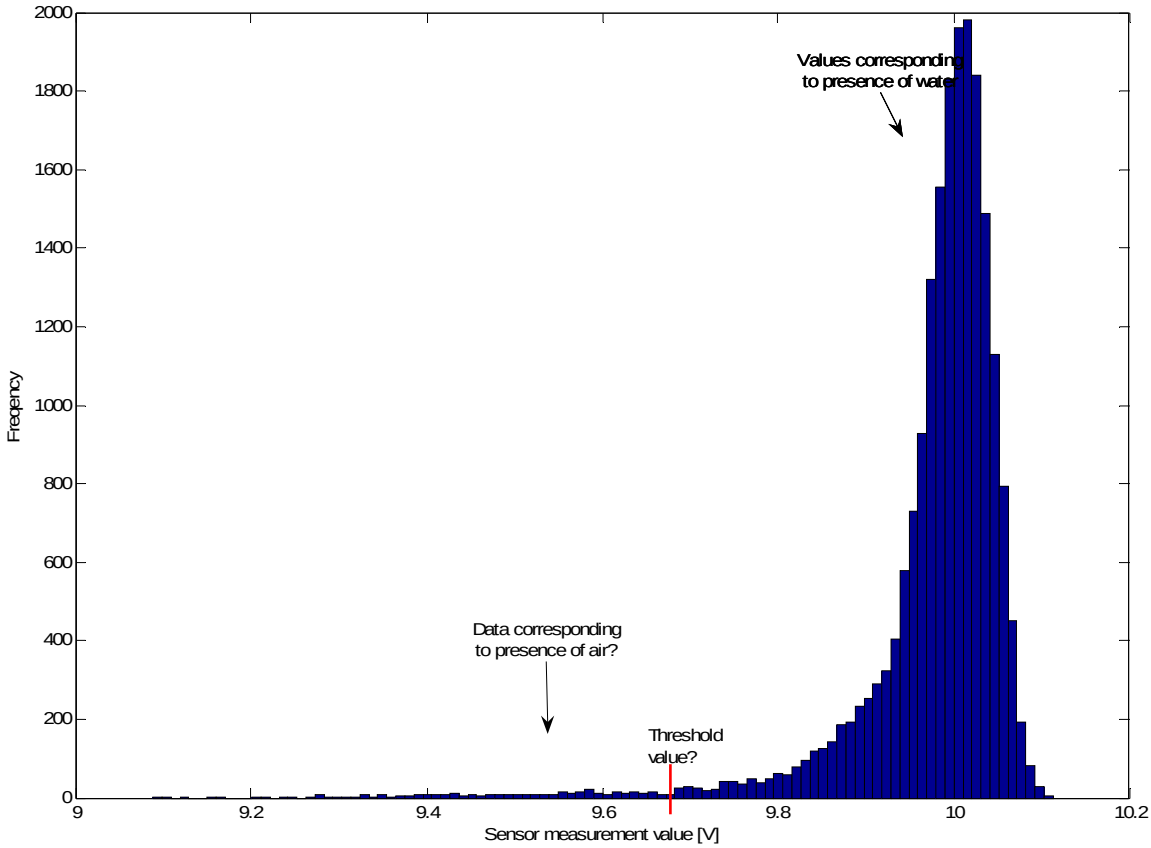

Figure 3.10: A histogram of measurements made with resistivity sensor 1 at an intermediate flow rate. An example of the actual signals is shown in Figure 3.2. From this figure it is hard to determine which signals correspond to presence of air and where to put the threshold value for the transition between the fluids.

The second method proposed here is to draw a threshold line that varies in time based on local variations in the signal. One advantage of using a method like this is that it might be useful in situations when the electrical properties of the fluid are changing in time (e.g. if the measurement tool is being lowered downhole and the amount of solvents in the fluid varies with depth). A simple example is chosen here for illustrative purposes where the threshold line is drawn as a one second moving average (note that the actual signal has also been filtered to remove the 60 Hz electrical noise). Figure 3.11 uses data from the phototransistor and Figure 3.12 uses data from the resistivity sensor (data taken from Pilot test 1).

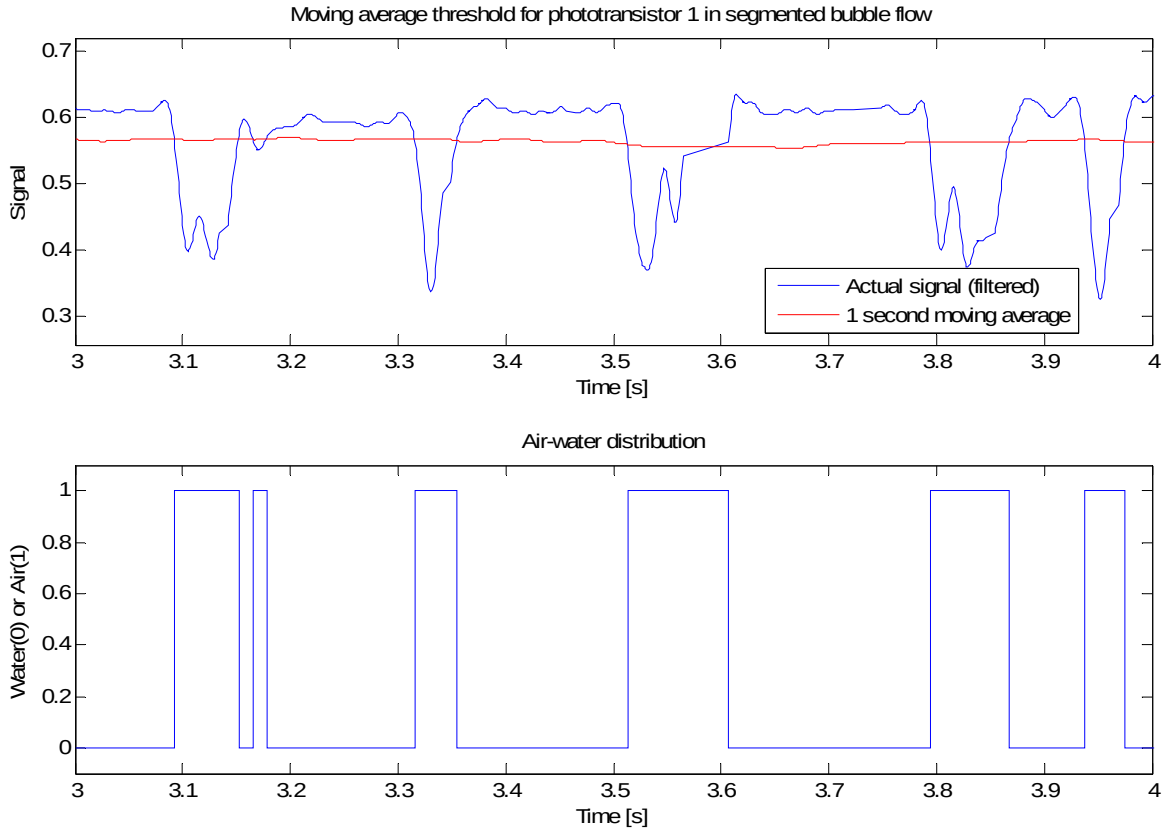

Figure 3.11: A moving average threshold used to determine whether the signal from a phototransistor corresponds to air or water.

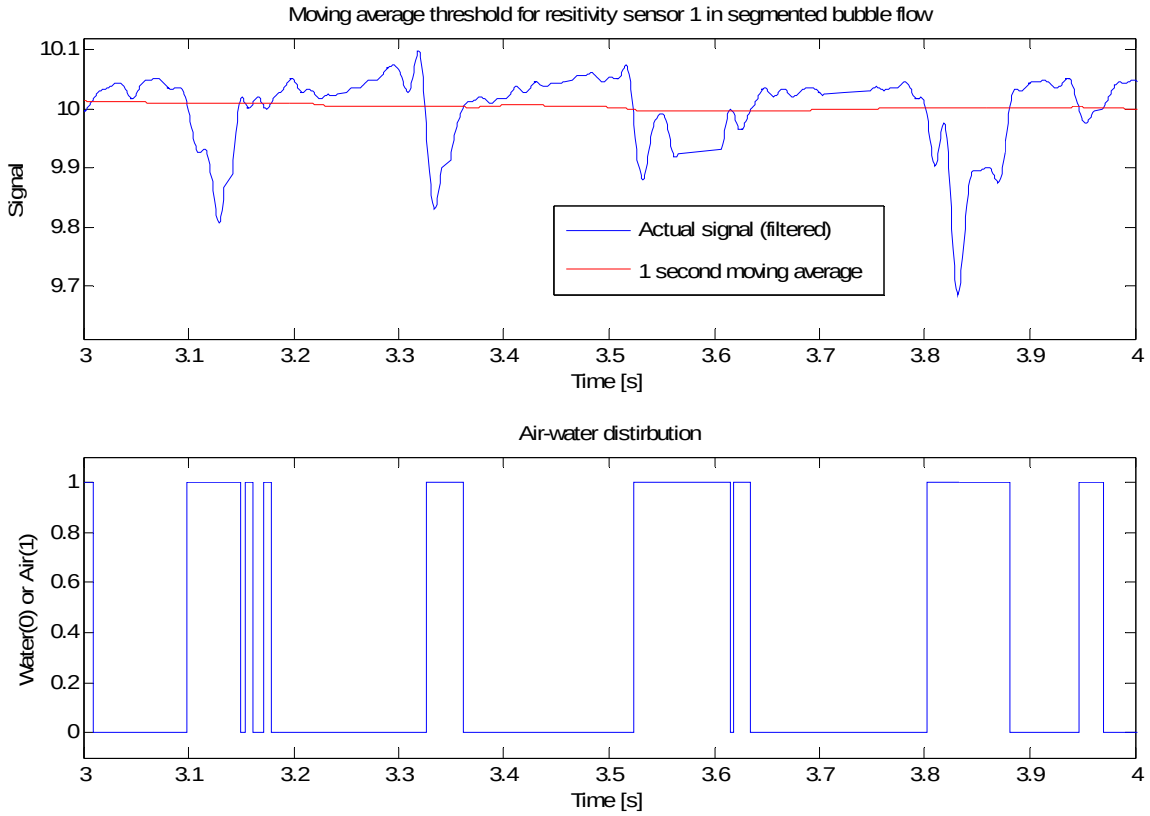

Figure 3.12: A moving average threshold used to determine whether the signal from resistivity sensor corresponds to air or water.

As indicated by Figures 3.11 and 3.12, a fairly accurate bulk estimate of the presence of bubbles is possible using this method. The bubble signals from the two sensors show a relatively good correlation and the calculated void fraction is 29.3% as calculated from the phototransistor 1 measurement but 31.1% using the resistivity sensor 1. Note also that because of the electrical noise in the resistivity measurement, it tends to estimate more frequent and smaller bubbles than does the phototransistor.

The moving average threshold method should work fairly well as long as the void fraction is in the middle ranges (say 20-80%), but as the limit of pure water or pure air is approached the method will cease to work because the moving average threshold will move to close to the signal of the dominant fluid. Hence, one would expect an underestimate of the dominant fluid.

Tables 3.1 to 3.3 summarize estimates of bubble velocity, average bubble length, void fraction and the number of bubbles counted over the measurement period for each of the three Pilot tests.

Table 3.1: Summarized results for calculated bubble flow properties from Pilot test 1.

Pilot test 1	Sensor:	Resistivity1	Resistivity2	Phototrans1	Phototrans2	STD
	Bbl Velocity [m/s]:	0.287	0.287	0.281	0.281	0.0038
	Avg Bbl Length [mm]:	6.5	5.4	9	8.6	1.7
	Void Fraction:	31.1%	27.6%	29.3%	30.8%	2%
	Number of Bbls:	279	296	184	203	55

Table 3.2: Summarized results for calculated bubble flow properties from Pilot test 2.

Pilot test 2	Sensor:	Resistivity1	Resistivity2	Phototrans1	Phototrans2	STD
	Bbl Velocity [m/s]:	0.181	0.181	0.179	0.179	0.0008
	Avg Bbl Length [mm]:	6.4	4.8	9.3	8.2	2.0
	Void Fraction:	27.4%	24.8%	20.1%	20.1%	4%
	Number of Bbls:	143	173	71	82	49

Table 3.3: Summarized results for calculated bubble flow properties from Pilot test 3.

Pilot test 3	Sensor:	Resistivity1	Resistivity2	Phototrans1	Phototrans2	STD
	Bbl Velocity [m/s]:	0.467	0.467	0.467	0.467	0.0000
	Avg Bbl Length [mm]:	8.2	9.2	12.8	10.3	2.0
	Void Fraction:	35.9%	49.6%	58.2%	54.9%	10%
	Number of Bbls:	378	464	392	459	45

Table 3.4 shows the measured flow rates and flow rate ratios measured using the simple flow meter described in the Quarterly Report from Spring 2005. Given the aforementioned assumptions for segmented flow, the ratio Q_{air}/Q_{tot} should equal the void fraction and hence we can compare the two values to get an estimate of the accuracy of these calculations. Some caution should be taken is the comparison since the uncertainty in the measurements from the flow meter is rather large.

Table 3.4: Measurement results from the simple flow meter described in the Quarterly Report from Spring 2005. The ratio Q_{air}/Q_{tot} can be compared to the void fractions reported in Tables 3.1 to 3.3. Note the relatively large uncertainty in the measurements made by the flow meter.

	Qair	dQair	Qwater	dQwater	Qair/Qtot	d(Qair/Qtot)
Pilot Test 1	1.15	0.61 (53%)	7.43	0.37 (5%)	0.13	0.09 (64%)
Pilot Test 2	1.41	0.32 (23%)	4.88	0.24 (5%)	0.22	0.07 (32%)
Pilot Test 3	12.58	0.73 (6%)	4.88	0.24 (5%)	0.72	0.08 (11%)

As might have been expected the moving average threshold method seems to work fairly well when the void fraction is at an intermediate value. This is seen in Pilot test 2. In Pilot test 1 the void fraction has become too low for a proper estimate to be made by this method and an underestimate of the water (the dominant fluid) is seen as expected. In the case of Pilot test 3, an underestimate of air is seen, which was not predicted by this simple model of the segmented flow, but this could perhaps be explained by turbulence and vibrational effects that the flow has on the electrode. Electrical noise and crosstalk could also play a role here.

3.3 FUTURE WORK

3.3.1 Full size application design

The Pilot Tests run until now have all been in 1/8 in. tubes with segmented air/water flow. It is now time to move over to a larger pipe (4 in.) and start experimenting with various sensor designs. Initially the goal is to design a sensor or sensor housing, which is sturdy but does not disturb the flow to much and enables accurate detection of the passing bubbles. Later in the project, issues concerning downhole applications need to be considered, e.g. heat, pressure and corrosion resistance.

3.3.2 Repeating the Pilot tests

Some time might be spent on repeating a test similar to the Pilot tests. This will probably only be done in to quickly test new ideas for improving the sensor or circuitry design. The data from such an experiment could quickly be analyzed by using a series of scripts and functions that have been written in MATLAB to for this purpose. The simple reference flow meter should also be replaced by a more reliable one, especially for the air flow. If a severely improved results can be obtained e.g. with less crosstalk or a higher signal-to-noise ratio, these new data could be used for further development of methods to calculate the void fraction and other properties of the flow.

3.4 CONCLUSION

A method utilizing the cross-correlation function has been applied successfully to measure the bubble velocity as a bubble passes two sensors spaced a known distance apart. Two methods to infer the void fraction have been investigated, but neither of them has brought completely satisfactory results. The root of the problem probably lies in the fact that the response time of the sensors is too slow. Also, in the case of the resistivity sensor, the signal-to-noise ratio is rather low and there is too much crosstalk between the two electrodes.

4. ELECTRICAL IMPEDANCE TOMOGRAPHY (*EIT*) METHOD FOR SATURATION DETERMINATION

This research project is being conducted by Research Assistant Robert Stacey, Senior Research Engineer Kewen Li and Prof. Roland Horne. The intent is to develop a method to measure core saturation using electrical impedance tomography (EIT). This method is being investigated because the X-ray CT scan technique has limitations on pressures and temperatures due to the strength of the plastic core holders available.

4.1 INTRODUCTION

The idea to measure the saturation distribution in a core using EIT was described in a paper by van Weereld, et al. (2001). The paper showed that EIT techniques were able to measure the saturation of a two phase system (oil and brine) in near real time. Therefore this method is being investigated further in order to better understand two-phase (steam water) systems.

4.1.1 Background

The idea behind EIT is that by imposing an electric current across an inhomogeneous medium, the distribution of the internal electrical impedance will result in a variation of voltage potential at the surface. Measurements of the variable voltage potential could be used to infer the resistivity distribution within the medium. This internal distribution of electrical impedance is translated into water saturation based upon the impedance distinction between the two phases. Figure 4.1 is a diagram of a typical two-dimensional EIT experiment, consisting of 16 electrodes with an imposed current I across the core Ω, and measurement of the resulting potential V_1.

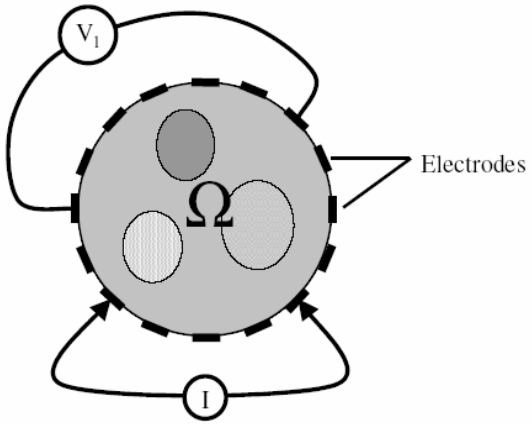

Figure 4.1: Diagram of Electrical Impedance Tomography experiment. The potential V_1 *is measured after a current* I *has been imposed across the core* Ω*. (Molinari 2003).*

The governing equation for EIT imposed upon a core Ω is:

$$\nabla \cdot (\sigma + \imath \varpi \varepsilon) \nabla \phi = 0 \tag{4.1}$$

Where σ is the electric impedance of the medium, ϕ is the electric potential, ϖ is the frequency, and ε is the electric permittivity. Under conditions where low frequency or direct current is used ($\varpi \approx 0$), Equation 4.1 can be reduced to the standard governing equation for EIT (Molinari 2003):

$$\nabla \cdot (\sigma \nabla \phi) = 0 \tag{4.2}$$

The EIT inverse problem can be simplified down to a system identification problem. The cause and effect (injected current ***I*** and measured voltage ***V***) are known, but the physical system is unknown (impedance distribution σ). The nonlinearity arises in σ, as the potential distribution ϕ is a function of the impedance, $\phi = \phi(\sigma)$, and we cannot easily solve Equation 4.2 for σ (Molinari 2003). The ill-posed nature of the problem is clearly apparent when observing the diffusive nature of electricity, coupled with the inherent measurement errors.

4.1.2 Research

The areas required to develop an effective EIT system can be separated into three main categories; electrode configuration and connection, data acquisition, and data processing. The latter two have been researched and developed in similar fields, particularly the medical field. Polydorides (2002) in particular has worked extensively in addressing the data processing issue of soft-field tomography, and has developed a MATLAB toolkit EIDORS exclusively for this problem.

The Electrical Impedance and Diffuse Optical Reconstruction Software (EIDORS) project has developed a community that promotes communication and sharing of software to further the development of EIT. The software, documentation, demonstrations and available help will be useful when data processing and volume visualization begins.

As for the data acquisition system, the experiment of van Weereld et al. (2001) required data collection from 192 electrodes simultaneously to produce near real-time images, and did so successfully. However, the optimum order and procedure in collecting data has been debated by Molinari (2003) and Polydorides (2002), both of whom have modeled the system at hand extensively, but have performed little physical experimentation. Polydorides (2002) has suggested that a 16 electrode ring is the optimum size based upon computational time, the noise imposed by additional electrodes, and the fraction of singular values that are useful. Another method of interest suggested by Polydorides (2002) is a segmented electrode configuration. For example four electrodes across from one another would be turned on simultaneously, while the remaining electrodes measure voltage independently. Molinari (2003) and Polydorides (2002) have many suggestions on techniques to reduce computational time, increase resolution, and filter out noise, but all of this will be applied and discussed in greater detail when data acquisition begins.

The major foreseen difficulty is in the electrode configuration and connections. In several papers (van Weereld et al., 2001, Polydorides 2002, and Molinari 2003) it has been found

that accurate, consistently geometric connections are difficult to obtain, and the practical limitations imposed by wiring limit the number attached by hand (van Weereld et al. 2001). A solution to this problem was to use a flexible circuit designed for the core specifically to ensure consistent size and distribution of electrodes while also creating a compact manageable system as compared to conventionally wired electrodes. However, to start the research, a conventional wiring scheme has been used to begin testing some of the data collection and processing schemes.

4.2 THE EIT APPARATUS

The primary idea behind the EIT apparatus, more specifically the electrode configuration, is that solid connections to the core sample must be made and the electrodes must be equidistant around the circumference of the core. This is in order to simplify the model used in solving the inverse problem. The design variations of the apparatus appear when trying to decide on a feasible number of electrodes, whether a flexible circuit is warranted and viable, and which design will be simple and reliable.

4.2.1 Electrode Design

The preliminary design decided upon is simple enough to eliminate many unnecessary problems, such as leaks from the system, short circuiting, and poor connections. Yet the system is large enough with three rings of 16 electrodes to test the data acquisition system and the MATLAB toolkit EIDORS in post processing. Figure 4.2 shows the preliminary design with three rings of 16 electrodes attached to the Berea sandstone core with conductive epoxy. This design will work by placing the base of the sandstone into water and allowing water to naturally imbibe by capillary forces. During this time the data acquisition system will be recording the field potential and calculating the internal impedance distribution. The idea is that visual observations of the saturation front can be used in assessing the EIT system and its performance.

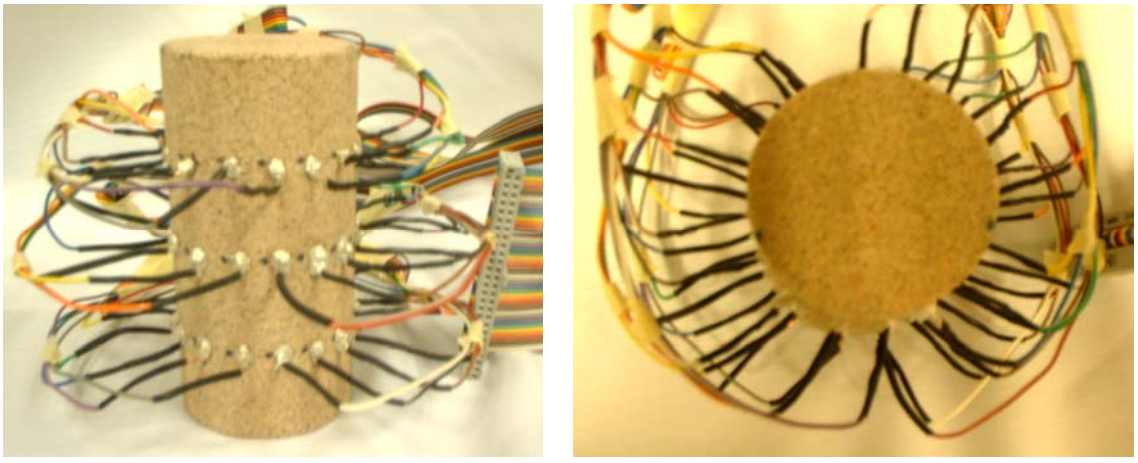

(Side View) (Top View)

Figure 4.2: Side and top view of the preliminary design. 48 electrodes were attached to a Berea sandstone core using conductive epoxy.

If the preliminary design is successful in proving that it is feasible to determine saturation with EIT, then the project will move forward to one of the mentioned future designs. The two foreseen options will allow for high pressure and temperature conditions along with pressurized phase transport through the core, just as in typical core experiments. However, the main point at which the designs diverge is whether to use a flexible circuit design or a modified rubber sleeve design. These two options will be investigated as the research continues.

4.2.2 Data Acquisition System

The basic requirements of the EIT data acquisition system were found to be very similar in the case of Polyrides, and van Weereld. The EIT system requires a computer with sufficient speed and memory to handle the data, a constant current source, and a matrix/multiplexer system that can handle the array of electrodes. Essentially the system must have the capability of measuring the voltage potential at all electrodes, while applying a designated current across a select set of electrodes. The system must then change the set of electrodes applying current and measure the voltage potential at the remaining electrodes. It is obvious that under such a situation many measurements must be taken and a high speed switching system is necessary. In our case with 48 electrodes, 2,304 switches need to be made. This is why National Instruments SCXI-1130 switch matrix was selected. The current numbering system for our core can be seen in Figure 4.3.

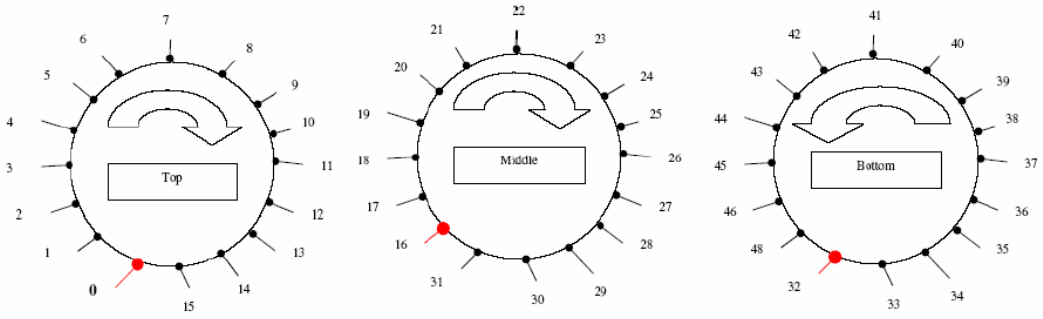

Figure 4.3: Numbering system for top, middle and bottom electrode plan.

The SCXI-1130 is set in a 4x64 (1-wire) configuration, meaning that 64 channels are crossed with four channels, giving the ability to access 64 channels from four channels. The present design will be using 4x49 channels, 48 electrodes with one ground crossed with one current source channel and three voltage measurement channels. The SCXI-1130 has the capability of scanning at a rate of 900 cycles per second, which corresponds to an estimated scan time of 2.5 seconds for the 48 electrode core. With a scan rate this fast it is anticipated that it will be possible to capture saturation fronts traveling through the core and it may also be possibly to reduce the noise present in the data by performing a time moving average.

Currently the total accuracy of our system is unknown, but some limitations and tolerances are known. The SCB-68 voltage measurements are precise to several hundredths of a volt, and can measure up to +/- 10 V. The limitations of concern deal with the switching matrix capabilities, as the applied current cannot exceed 400mA, and the voltage my not exceed 30 Vac, and the 37 switching rate is limited to 900 cycles/minute. These must be kept in mind when designing test runs in the future in order to protect the equipment and obtain accurate results.

A schematic of the actual EIT apparatus can be seen in Figure 4.4. The matrix will be controlled by the VI developed in LabView on the computer. The voltage potential data will be acquired using LabView with the DAQ card. The collected data will then be processed in the MATLAB program developed by the EIDORS project.

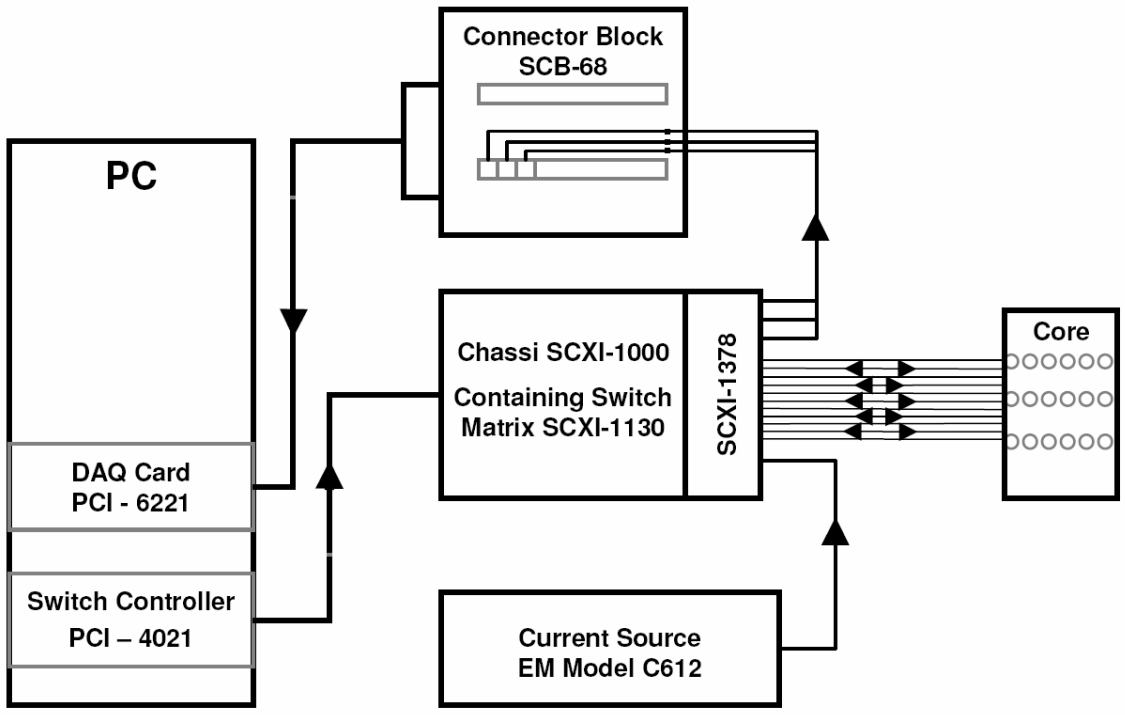

Figure 4.3: The present EIT system schematic. The PC cycles through the core through the switch matrix by measuring the voltage potential at every electrode before changing the current source electrodes. The current source is supplied by a constant current source, while the voltage potential measurements are retrieved by the DAQ card.

4.2.3 Data Processing

The data processing portion of the experiment has not been done with experimental data yet, but data generated in the EIDORS demo project has been processed (Figure 4.4). This demo consisted of a cylinder 3 units tall with a radius of 1 unit. Two rings of 16 electrodes are placed around the cylinder and a finite mesh created for this geometry is used. The resistivity coefficients in two areas are assigned in the finite mesh, Figure 4.4 (a, b). This configuration is solved as a forward problem to generate the voltage potential measurements, and prior to being used to solve the inverse problem a factor to generate Gaussian noise in the data is applied. This is done to imitate actual experimental data, and allow for a feel for the effects of electrical noise. The inverse solution can be seen in Figure 4.5 (c-l). The effects of electrical and numerical noise are observed clearly. The diffusive nature of the problem greatly reduces the detection of sharp contrasts in materials and this problem will be addressed through solution and measurement methods.

The inverse problem can be solved using two methods within EIDORS. The first approach is the Gauss-Newton method. It involves eliminating the second derivative in the Taylor expansion of the nonlinear forward problem, creating a generalized inverse of the Jacobian and inverting the well-posed problem with the Newton-Raphson method. The second method considers a linearised form of the inverse problem and then adopts a Tikhonov type regularization to obtain a step solution within the Newton-Raphson method (Polyrides 2002).

One step that Polyrides suggests that deserves attention is that of the finite-element mesh used in solving the inverse problem. The demo program uses a relatively course mesh with 928 measurements. In our case we will be using approximately 2,300 measurements, increasing the computational time significantly. Therefore attention must be made in creating the mesh; the mesh density at the electrodes must increase to take into account the influence of the electrodes to reduce iterative solver time. However, the mesh will evolve with the rest of the experiment, towards less computational time and greater accuracy.

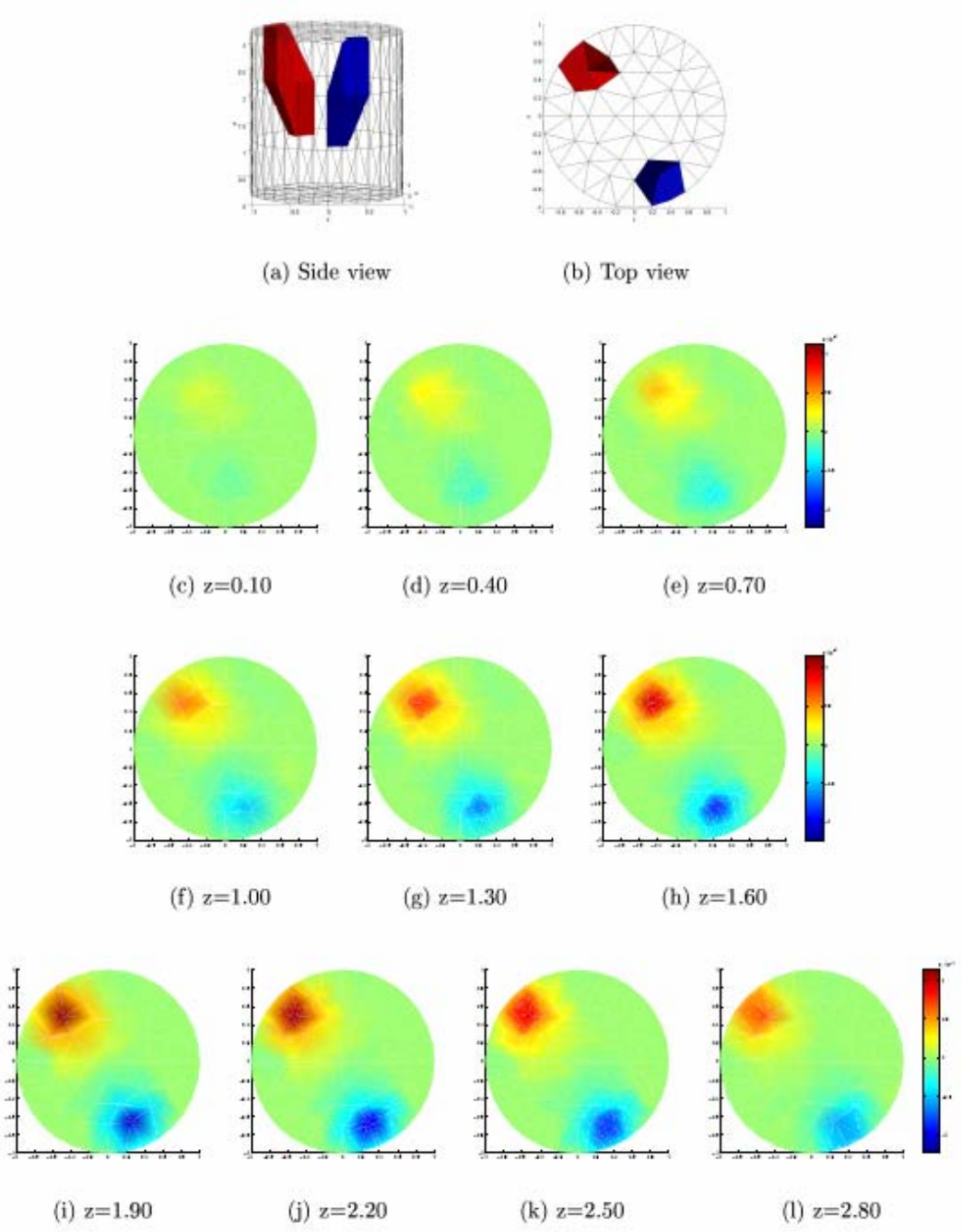

Figure 4.4: EIDORS demo program results. Images a and b are views of the cylinder core created with assigned resistivity values in two regions. This is used to generate the voltage potential data. Images c-l are cross sections of the inverse solution. (Polyrides 2002)

4.3 EXPERIMENTAL RESULTS

The approach used has been to perform small experiments systematically to ensure we understand how the equipment works, what values we should expect, and of course to identify the problems within the apparatus.

4.3.1 Preliminary Results

We have moved to the next step of using a DC constant current generator and the data acquisition system after the first saturation front was detected by simply applying a DC current across the core, and measuring the voltage potential at two electrodes during the imbibition process. Initially the new constant current system had a stray current present of several volts that essential overshadowed any DC voltages measured on the core. This problem was solved after extensive troubleshooting by applying proper grounding and a Faraday cage. Now the induced noise in the system is less than 0.03 volts, allowing accurate, precise, instantaneous voltage measurements upon the core.

Applying a 10 mA current across the saturated Berea sandstone with approximately 10 volts resulted in a smooth symmetric voltage distribution observed by the potential at the electrodes. However, an interesting phenomenon was observed, the voltage field in the system climbed steadily with time. van Weereld et al., (2001) observed this issue as well with their EIT apparatus. They showed that this phenomenon occurs because the electrode in contact with the brine forms an electrochemical interface, essentially acting as a capacitor. It was found that to address this issue the direction of the DC current must be reversed for each measurement, termed a "bipolar DC pulse". van Weereld also points out that applied voltages and current times must be taken into account with the brine solutions to avoid electrochemical effects.

4.4 CONTINUING AND FUTURE WORK

Currently we are working towards finishing the automated switching and logging program for the data acquisition system. The current goals of the program are to automate the voltage and current switching, such that we essentially 'scan' the core with a "bipolar DC pulse" technique, and to have a data logging system. The exact process of scanning will be addressed in the near future as Molinari (2003) and Polydorides (2002) have many suggestions on techniques to reduce computational time, increase resolution, and filter out noise, but all of this will be applied and addressed in greater detail as data acquisition and visualization begin.

With the data finally collected, they will first be analyzed by standard techniques before being visualized to check if the voltage distribution is reasonably free of noise and follows anticipated voltage trends over time. The data will then be processed in the EIDORS Matlab package for visualization, after the finite element grid for the core has been constructed.

The long term goals for this project are to verify saturation measurements obtained with the EIT system with CT scanner saturation measurements, and to implement a high pressure and temperature column so that experiments at reservoir conditions can be performed.

5. REFERENCES

Archie, G.E.: "The Electrical Resistivity Log as an Aid in Determining Some Reservoir Characteristics," AIME Petroleum Tech. (1942), 1-8.

Cheremisinoff, P.N., Cheremisinoff, N.P.: "Flow Measurement for Engineers and Scientists", Marcel Dekker, inc, 1988. p. 101-130

Crow, C.T., Sommerfeld, M., Tsujinaka, Y., "Multiphase Flows With Droplets and Particles", CRC Press, 1997. p. 309

Horne, R.N., Reyes, J.L.P., Li, K.: "Estimating Water Saturation at The Geysers Based on Historical Pressure and Temperatue Production Data by Direct Measurement," Final Report to California Energy Comission, June 2003.

Horne, R.N., Satik, C., Mahiya, G., Li, K., Ambusso, W., Tovar, R., Wang, C., and Nassori, H.: "Steam-Water Relative Permeability," presented at World Geothermal Congress, Kyushu-Tohoku, Japan, May 28-June 10, 2000; GRC Trans. 24 (2000).

Li, K. and Horne, R.N.: "An Experimental and Theoretical Study of Steam-Water Capillary Pressure," *SPEREE* (December 2001), p.477-482.

Li, K. and Horne, R.N.: "A Semianalytical Method to Calculate Relative Permeability from Resistivity Well Logs," SPE 95575, the 2005 SPE Annual Technical Conference and Exhibition, Dallas, TX, USA, October 9-12, 2005.

Longeron, D.G., Argaud, M.J., and Bouvier, L.: "Resistivity Index and Capillary Pressure Measurements under Reservoir Conditions using Crude Oil," SPE 19589, presented at the 1989 SPE Annual Technical Conference and Exhibition, San Antonio, TX, USA, October 8-11, 1989.

Molinari, M.: *High Fidelity Imaging in Electrical Impedance Tomography*, Ph.D. dissertation, University of Southampton, Southampton, United Kingdom (2003).

Persoff P. and Huken J. B. "Hydrologic characterization of four cores from the Geysers coring project" Proceedings of the 21st workshop on Geothermal Reservoir Engineering Stanford University Jan 22-24 1996 p.327-333

Phogat V. K. and Aylmore L. A. G. "Computation of hydraulic conductivity of porous materials using computer assisted tomography." Aust. J. Soil. Res. 24, 071-8, 1996

Polydorides, N.: *Image Reconstruction Algorithms for Soft-Field Tomography*, Ph.D. dissertation, University of Manchester, Manchester, United Kingdom (2002).

Reyes J. L. P., Li K., Horne R N. " Estimating Water Saturation at the Geysers Based on Historical Pressure and Temperature Production Data and by Direct Measurement" California Energy Commission Report 2003.

Szabo, M.T.: "New Methods for Measuring Imbibition Capillary Pressure and Electrical Resistivity Curves by Centrifuge," SPEJ (June, 1974), 243-252.

Toledo, G.T., Novy, R.A., Davis, H.T. and Scriven, L.E.: "Capillary Pressure, Water Relative Permeability, Electrical Conductivity and Capillary Dispersion Coefficient of Fractal Porous Media at Low Wetting Phase Saturation," SPE Advanced Technology Series (SPE23675), 2(1), 136-141, 1994.

van Weereld, J.J.A., Player M.A., Collie, D.A.L, Watkins, A.P., Olsen, D.: "Flow Imaging in Core Samples by Electrical Impedance Tomography," paper SCA 2001-06, Society of Core Analysts.